Insights from Local Network Structures and Localized Diffusion on the Ease of Lithium Ion Transport in Two Mixed Glass-Former Systems

Kristina Sklepić[1], Radha D. Banhatti[1,*], Gregory Tricot[2], Petr Mošner[3], Ladislav Koudelka[3],

Andrea Moguš-Milanković[1]

[1]Division of Materials Chemistry, Ruder Boskovic Institute, 10000, Zagreb, Croatia,

[2]LASIR UMR-CNRS 8516, Université de Lille, Sciences et Technologies, Villeneuve d′Ascq F-59655, France

[3]Department of General and Inorganic Chemistry, University of Pardubice, Faculty of Chemical Technology, 53210 Pardubice, Czech Republic

ABSTRACT

The conductivity enhancement observed in the two glass systems, **A**: $40Li_2O-(60-x)P_2O_5-xGeO_2$ and **B**: $40Li_2O-10B_2O_3-(50-x)P_2O_5-xGeO_2$, as germanate content is increased from 0 to 25 mol% confirms the positive mixed glass-former effect (MGFE) in these systems. In this study, we further employ state-of-art NMR techniques along with Raman spectra to probe the local network structures. We use the MIGRATION concept to model the experimental conductivity and permittivity spectra obtained from impedance spectroscopy to understand scaling features of spectra and to calculate the value of the spatial extent of the localized diffusion of the lithium ion. As x increases from 0 to 25 mol%, for system A, a continuous increase of the POGe cross linkages as well as a continuous and strong modification of the phosphate network is observed. In system B, deeper analysis of the ^{31}P MAS-NMR experiments done using 2D $^{11}B/^{11}B$ homo-nuclear and $^{11}B/^{31}P$ hetero-nuclear NMR is used to determine the nature of the BOB linkages as well as that of POB linkages. Modelling of the conductivity spectra shows that the shape parameter of the spectra remains the same for both systems and for all compositions, a feature typical for MGFE. Further, correlating the trends of the spatial extent of localized diffusion with that gleamed from the local structures, we infer that as relative germanate content increases, in the ternary glass (system A) the ease of mobility of the Li^+ ion is enhanced while in the quaternary glass (system B, x > 0) it is somewhat hindered.

1. Introduction

The field of amorphous solid electrolytes has developed enormously in the last hundred years[1,2] and research on lithium based energy storage systems is focused on technological applications.[3-5] In parallel, efforts are ongoing in understanding factors that influence ion transport in a glassy

matrix.[6,7] One of the striking features of glassy ionic conductors is that both mobile ion concentration and glass composition, as well as its structure majorly affect the resulting conductivity.[8-10]

In search for oxide-based materials that are both stable for solid-state device applications and highly conductive, mixed-glass former (MGF) systems were discovered in 1985 when Magistris et al. replaced B_2O_3 by P_2O_5 in a lithium borate glass.[11] Studies on MGF systems with a high (40 to 50 mol%) but constant alkali oxide content showed that they exhibited few marked features hitherto unobserved in single or mixed alkali ion conductors. *Firstly,* the glass transition temperature, T_g, and the DC conductivity, σ_{DC}, show similar trends as a function of relative former content.[11-13] *Secondly,* structural studies using X-ray photoelectron (XPS) spectroscopy[14] showed that based on alkali content, the alkali (in these studies, the Li^+) ion was found associated with the non-bridging oxygens (NBOs) of different structural groups. *Thirdly,* σ_{DC} is enhanced as a function of relative compositions of the network formers, and its magnitude at the maxima was higher than those of the two binary systems. Since it was also higher than that for binary systems with higher alkali content,[13-14] the MGFE cannot be explained using the weak electrolyte model.

Recently, a renewal of interest in MGFE was triggered when sodium borophosphate glasses $(0.4Na_2O-0.6(xB_2O_3-(1-x)P_2O_5))$, x varying from 0 to 1, were investigated in great detail by using a combination of Raman, solid state nuclear magnetic resonance (NMR) and impedance spectroscopy techniques.[15-16] The trend of the increase of the B^{4-} tetrahedral, quantified as percentages of the various structural units, showed perfect correlation with the trend of nearly two orders of increase in the magnitude of the DC conductivity.[15] Conductivity and permittivity spectra from impedance spectroscopy were also analyzed and modelled[16,17] to extract relevant length-scales related to sodium ion transport. The trend displayed by the spatial extent of localized

diffusion of the sodium ions was same as the trend observed in DC conductivity and structure, clearly demonstrating that MGFE is closely related to the microscopic aspects of ion-network interaction.

Following this path-breaking work,[15-16] a large body of work on structural and electrical properties on MGF systems has ensued.[18-35] The main bulk of these studies has been on alkali borophosphate glasses,[18-29] and also some work on germanophosphate glasses.[30-35] Additionally, there has been some efforts in extracting relevant length scales (see Appendix A) by analyzing the ionic conductivity and dielectric permittivity spectra in alkali ion based MGF systems.[17,36-38]

The main findings on changes in structural units and bonds as a function of relative composition of glass formers in *borophosphate glasses* containing Li_2O or Na_2O as network modifiers is that hetero-atomic bonds such as P-O-B are preferred to homo-atomic bonds such as P-O-P and B-O-B, for up to about 30 mol% borate content. This information was made possible by X-Ray Diffraction (XRD) technique and XPS spectroscopy,[27] or by using Raman and magic-angle spinning (MAS) NMR experiments.[15,18-23,25-27] Further, it was shown that B^4 introduction induces the formation of $B(OP)_4$ structural units that increase the global glass network reticulation.

In recent years, an in-depth analysis of structural aspects have become possible due to the development of high field spectrometer allowing for highly resolved ^{11}B NMR analysis and novel correlation NMR techniques[39-40] – see also a latest and exhaustive review[41] and references therein. The local order of the borate species could be deeply analyzed and the NMR experiments allowed for a clear distinction between the tri- and tetra-coordinated borate species but also clearly discriminated between different B^4 units.[20] 2D correlation NMR was also used to analyze the medium range organization. Presence of BOB bonds was monitored through the edition of 2D

[11]B/[11]B map with the double quantum - single quantum (DQ-SQ) NMR technique and POB[4] and POB[3] linkages were highlighted by dipolar and scalar 2D [11]B/^{31}P correlation maps.[29]

For germanophosphate systems although a similar analysis with novel techniques will be highly informative, it is not possible to obtain direct information on Ge^4/Ge^6 proportion. It is well known that even in binary germanate glasses, there is a tendency for the germanium ion to form octahedral coordination with oxygen in addition to the tetrahedral coordination and an increase of NBOs. This is known as germanate anomaly.[42] However, it is also known from literature that octahedral coordination is not stable at more than 20 mol% alkali oxide content, while NBOs continue to increase.[43] In pure MFG systems presence of octahedrally coordinated germanium has been confirmed.[30,33] However, IR, Raman and ^{31}P MAS NMR investigations over wide range of compositions and temperature in lithium germanophosphate glasses have shown evidence for the formation of the $[GeO_{6/2}]^{2-}$ only for those composition with low lithium content and high germanate content.[31]

Recently, using high-energy X-Ray photons in diffraction (HEXRD) on a synchrotron and neutron diffraction on a spallation source, Hoppe et al.[34] have detected six coordinated Ge in the structure of Na_2O-GeO_2-P_2O_5 glasses with high P_2O_5 contents and up to 24 mol% GeO_2 fraction. Using thermal analysis, Raman, ^{31}P-MAS NMR and ^{23}Na NMR spectroscopy in the system $(M_2O)_{0.33}[(Ge_2O_4)_x(P_2O_5)_{1-x}]_{0.67}$ (M = Na, K) Behrends & Eckert[35] infer that at low Ge_2O_4 contents (x = 0.2), the structure is dominated by pyrophosphate chains and unmodified Ge-O-Ge bonded four-membered ring units. At higher germanate contents hetero-atomic P-O-Ge linkages dominate. In general, it is found that the phosphate network is modified by the alkali ion preferentially, resulting in partially clustered cation distributions. The authors conclude that their study provides only an indirect confirmation of the germanate anomaly.

In the current work, we consider the following two MGF systems. System A: $40Li_2O-(60-x)P_2O_5-xGeO_2$ glasses and system B: $40Li_2O-10B_2O_3-(50-x)P_2O_5-xGeO_2$ glasses, x = 0 to 25 mol%. It is evident that compositions of system B for x > 0 mol% are quaternary glasses, and are more complex than the usually studied ternary MGF systems. Both systems offer us the possibility to examine the role that cross linkages of the kind POGe or the Ge^4/Ge^6 proportion play in ion dynamics. *The main motivation* for this study is thus to examine the local network structures both in the absence and presence of borate units and examine the influences they have on the localized ion dynamics. This would enable us to explain the observed trends in DC conductivity in a simple manner despite the inherent complexity of the MGF systems chosen. Toward this we put to use the exciting combination of state-of-art NMR protocols and modelling of conductivity spectra as follows:

a) By using ^{31}P NMR MAS studies on system A we provide a quantitative analysis of the cross links between the phosphate and germanate chains in glasses with high mol% lithium ion concentration. This helps in understanding the progressive changes in the phosphate network as the germanate content is increased. We hope also to gain indirect information on the coordinate states of germanium ion.

b) Detailed results of thermal, Raman and conductivity measurements for system B has been published in Ref. 44. However, here by employing the new NMR techniques,[40] namely, combination of 1D/2D $^{31}P/^{11}B$ solid state NMR performed at high magnetic field (18.8 T) we provide a detailed analysis of both local and medium range orders.[20,29] This helps examine the cross linkages and the modification of structural units in the base phosphate glass as 10 mol% of phosphate is replaced by borate. The changes in the borophosphate network as germanate content is increased are then examined.

c) By using the model called the MIGRATION concept (an acronym for MIsmatch Generated Relaxation for the Accommodation and Transport of the IONs), we construct scaled representations of conductivity and permittivity spectra of experimental isotherms.[7,45] The spatial extent of localized diffusion of the mobile ion can then be calculated within this model for each composition in both systems. This is typically a material property, and the trend it displays[17,45-46] as a function of relative germanate content could help us understand how the changes in network structure can be correlated to the local excursions of the ion; increase (decrease) in local excursions would imply shallow (deep) potential wells, which in turn could facilitate (hinder) ion mobility.[17]

The article is structured as follows. Section 2 deals with experimental methodology. Section 3 gives a brief overview of the model, the MIGRATION concept, and the extraction of the relevant length scale. Section 4 is on results. These are presented concisely in the main text, while some additional details are provided in Supplementary information (SI). In Section 5, we discuss at length the various influences the local network structure has both on the localized diffusion and on the ionic mobility, and present our inferences on their impact on the diffusive ion dynamics in the two systems.

2. Experimental

2.1 Sample Preparation and Characterization

Glasses in the system $40Li_2O-(60-x)P_2O_5-xGeO_2$ ($0 \leq x \leq 25$ mol%) were prepared from analytical grade Li_2CO_3, H_3PO_4 and GeO_2 in batches of 10 g using Pt crucible. First, the homogenized starting mixtures were slowly heated up to 600°C for 2 hours to remove water and then melted in covered Pt crucible at 1100-1200°C. After 15 minutes heating at this temperature, the obtained melt was poured into pre-heated graphite molds to form suitable glass blocks.

Obtained glasses were annealed for 30 minutes at a temperature below their glass transition temperature and then slowly cooled to room temperature to improve their mechanical properties. The vitreous state was checked by XRD.

The glass density, ρ, was determined by the Archimedes method. The method relies on comparing weights of bulk samples in the air and in an immersion liquid. As an immersion liquid toluene is used. The molar volume, V_M, was calculated using the expression $V_M = M/\rho$, where M is the molar weight of the glass. These are presented in Table 1. For system B, the procedure is similar, and for details see Ref. 44.

The study of the thermal behavior of glasses was carried out for system A using the differential thermal analysis (DTA) with the equipment DTA 404 PC (NETZSCH) operating in the DSC mode. Measurements were carried out at the heating rate 10°C min^{-1} under a flowing atmosphere of N_2 on powdered glasses (100 mg, $d_{50} \sim 8$–10 μm) in an open Pt crucible. Details of dilatometric measurements on the bulk samples in the temperature range of 150-250°C, and details of recording the Raman spectra on bulk samples in the range 1400-200 cm^{-1} for system A is same as that done for system B and is described in Ref. 44.

Table 1. Composition, density, ρ, and molar volume, V_M, of the 40Li$_2$O-(60-x)P$_2$O$_5$-xGeO$_2$ glasses.

Li$_2$O / mol%	P$_2$O$_5$ / mol%	GeO$_2$ / mol%	$\rho \pm 0.02$ / g cm^{-3}	$V_M \pm 0.5$ / cm^3 mol^{-1}
40	60	0	2.31	42.0
40	55	5	2.40	39.7
40	50	10	2.52	37.1
40	45	15	2.64	34.7
40	40	20	2.77	32.4
40	35	25	2.87	30.6

2.2 NMR studies

The ^{31}P MAS-NMR experiments performed on system A (Li$_2$O-GeO$_2$-P$_2$O$_5$) were obtained at 162.9 MHz on a 9.4 T Bruker spectrometer. The experiments were acquired on a 4-mm probehead operating at a spinning frequency (ν_{rot}) of 12.5 kHz with a 2.5 μs pulse length (corresponding to a $\pi/4$ flip angle), 16 accumulations and a recycle delay (rd) of 120 s. The ^{31}P and ^{11}B MAS-NMR experiments performed on system B (Li$_2$O-B$_2$O$_3$-GeO$_2$-P$_2$O$_5$) system were obtained at 324.0 and 256.8 MHz on a 18.8 T Bruker spectrometer using a prototype 3.2-mm ^{11}B/^{31}P probe operating at ν_{rot} = 20 kHz. The 1D ^{31}P MAS-NMR experiments were obtained with a 2.5 μs pulse length (corresponding to a $\pi/4$ flip angle), 48-96 accumulations and a rd of 180 s. The ^{11}B MAS-NMR analyses were acquired with a 1 μs pulse length (corresponding to a $\pi/12$ determined on a liquid), 2048 accumulations and a rd of 2 s. The spatial proximity between the phosphate and borate species were analyzed with the 2D ^{11}B(^{31}P) D-HMQC NMR sequence.[40] A ^{11}B $\pi/2$-τ-π-τ selective spin-echo, recorded with a 18 μs length π pulse, is modulated by two 4 μs length $\pi/2$ pulses applied

on ^{31}P. The heteronuclear dipolar interaction is recoupled using a 1 ms length SR4$^2_1$ pulse scheme on the ^{31}P channel. As demonstrated recently,[29] the short recoupling time used here allowed discussing the spatial proximity observed in the 2D map in terms of chemical connectivity. The 1024 x 22 acquisitions points were recorded under rotor-synchronized conditions (ν_{rot}= 20 kHz) with 256-512 accumulations and 2 s rd. The 2D ^{11}B/^{11}B maps were edited with a DQ-SQ NMR sequence specifically designed for quadrupolar nuclei.[39] The 2048 x 70 acquisition points were recorded at ν_{rot} = 20 kHz, under rotor-synchronized conditions and the homonuclear dipolar interaction was recoupled during 200 µs using a BR2$^1_2$ recoupling scheme composed of two R2$_1^2$ pulse schemes followed by two R2$_2^{-1}$ pulse schemes. Each t1 step was acquired with 256 accumulations and a rd of 2s. The ^{11}B and ^{31}P chemical shifts were referred to NaBH$_4$ and H$_3$PO$_4$ as -42.06 and 0 ppm, respectively.

2.3 Electrical properties

Samples for electrical properties measurements were cut from annealed bars into ~1 mm thick disks and polished. Gold electrodes, 7 mm in diameter, were sputtered onto both sides of the samples using Sputter Coater SC7620. Samples were stored in a desiccator until measurements were performed. Electrical and dielectric properties were obtained by measuring complex impedance using an impedance analyzer (Novocontrol Alpha-AN Dielectric Spectrometer, Novocontrol Technologies GmbH & Co. KG, Germany) over the frequency range from 0.01 Hz to 1 MHz and in the temperature range from 183 K to 523 K. The temperature was controlled to an accuracy of ±0.2 K. Details of equivalent circuit modelling used to analyze the impedance spectra are discussed in Ref. 44. The values of the resistance obtained from the fitting procedures, R and electrode dimensions (d is sample thickness and A is electrode area) were used to calculate the DC conductivity, $\sigma_{DC} = d/(R \times A)$. In this work, as the focus is on examining the scaling features

of the conductivity and permittivity spectra of both systems A and B, no further equivalent circuit analyses are presented.

   3. Modeling Experimental Conductivity Spectra using the MIGRATION Concept

MIGRATION concept,[7,45] belongs to the class of jump relaxation models[47-48] which was originally developed by K. Funke. It uses a simple but realistic physical picture to describe the relaxation processes that ensue as a function of time in structurally disordered materials after an ion hops from its site at t = 0 to a neighboring site (*see, Leitmotif,* Appendix B).

A time-correlation factor, $W(t)$, that gives the probability that the hop is still successful, is defined. This function helps describe relaxation along the single-particle route. Concurrently, along the many-particle route, relaxation begins. This is governed by the decay of a mismatch function, $g(t)$. This mismatch function represents the normalized dipole-moment and is a measure of the dipole field generated by the hop of the "central" ion. Neighboring mobile ions respond to this field, and over time both its range and magnitude decays. The first rate equation ensues from the condition that the rate of decay of $W(t)$ needs to be proportional to the decay of the mismatch-function, $g(t)$. Two further equations are set up using the boundary conditions at $t = 0$ and as $t \rightarrow \infty$. Since these are coupled equations, they can be solved to yield a solution for $W(t)$, in a scaled notation for $W_s(t_s)$. See, *Formulation of the Model,* Appendix B.

The model scaled conductivity spectra in the frequency domain (see, *Connection to Conductivity Spectra*, Appendix B) is then constructed using the equations:

$$\sigma_s(\omega_s) = \frac{\sigma(\omega_s)}{\sigma_{DC}} = 1 + \omega_s \cdot \int_0^\infty (W_s(t_s) - 1) \cdot \sin(\omega_s t_s)\, dt_s \qquad (1)$$

$$\varepsilon_s(\omega_s) = \frac{\varepsilon_0 \omega_O}{\sigma_{DC}} \cdot \left(\varepsilon(\omega_s) - \varepsilon(\infty)\right) = \int_0^\infty (W_s(t_s) - 1) \cdot \cos(\omega_s t_s)\, dt_s. \qquad (2)$$

Note that the first equality in both Eqs. (1) & (2) gives a procedure to scale the experimental isotherms to yield a scaled spectrum. The next two equalities describe how each of these scaled

spectra can be reproduced as model spectra. In Eqs. (1) & (2), the quantity $\omega_S = \omega/\omega_O$, is the scaled angular frequency and ω_O is the angular-frequency where the conductivity dispersion sets in. Other quantities of the first equality in Eqs (1) & (2) are explained below using two model-free approaches to scaling experimental conductivity spectra.

In the first approach, the real part of the conductivity is plotted as $\log[(\sigma(\nu)T/(\sigma_{DC}\,T)]$ vs $\log[\nu/(\sigma_{DC}T)]$. In glasses with sufficient concentration of mobile ions, this typically yields a scaled spectrum. This scaling procedure due to Summerfield[49] implies time-temperature superposition. Thus, the only effect of temperature as it decreases (increases) is to slow down (speed up) the mobility of ions without any change of the mechanism of ion transport. Scaled permittivity spectra can be similarly generated by plotting $[(\varepsilon(\nu) - \varepsilon(\infty))] \cdot T$ vs $\log[\nu/(\sigma_{DC}T)]$. Here, $\varepsilon(\infty)$ is the permittivity due to faster electronic relaxation processes and not related to the slower relaxation processes connected with ionic hopping. This is another form of Summerfield scaling since hopping part of conductivity and permittivity are related to each other as: $\hat{\sigma}_{hop} = i\omega\varepsilon_0\hat{\varepsilon}$, where the hat over the two quantities represent that they are both complex quantities.

However, when concentration of mobile ions in a glass is very low, the average hopping length of the mobile cation can be large and can vary as a function of mobile ion concentration. In such a case, Summerfield scaling may not work. The quantity, $\varepsilon_0 \cdot \Delta\varepsilon/\sigma_{DC}$ was used by Sidebottom[50] in scaling conductivity and permittivity spectra. Here, $\Delta\varepsilon = \varepsilon(0) - \varepsilon(\infty)$ is the "dielectric strength of relaxation" and the ratio as defined is called the Sidebottom time, t_{SB}, as it has the dimension of time.

What is evident from Eqs. (1) & (2) is that the model spectra generated by MIGRATION concept contain both aspects of Summerfield and Sidebottom scaling features.

It is now possible to make a direct connection between the scaled low-frequency plateau and the localized displacement. From Eq. 2, one can write

$$\varepsilon_s(0) = \omega_O \cdot t_{SB} = \int_0^\infty (W_s(t_s) - 1)\, dt_s. \tag{3}$$

In terms of $\varepsilon_S(0)$, the spatial extent of localized diffusion can be written as:

$$\langle r_{loc}^2(\infty) \rangle = \frac{6 k_B \sigma_{DC} T}{N_v q^2} \cdot \frac{\varepsilon_S(0)}{\omega_O} \tag{4}$$

See, *Estimation of Spatial Extent of Localized Diffusion*, Appendix B for details.

The experimental spectra are modelled and scaled as follows: Firstly, using model spectra with various values of K, but arbitrary large value of B and with $N(\infty) = 0$, (see, *Parameters of the Model,* Appendix B), the model spectrum is superimposed on an experimental conductivity isotherm. The information needed for this is the DC conductivity, σ_{DC}. Once a proper choice of shape parameter K is made that reproduces the shape of any one experimental isotherm, the parameter ω_O that marks the onset of conductivity dispersion is determined precisely for each conductivity isotherm. Using ω_O and σ_{DC}, and using the first relation indicated in Eqs. (1) & (2), scaled conductivity and permittivity spectra are generated for each composition. The model permittivity spectrum that reproduces the scaled experimental permittivity spectra is generated using a suitable value of the parameter $N(\infty)$ yielding the value of the experimental $\varepsilon_S(0)$ plateau, the error being about 5% or less. The value of the spatial extent of localized diffusion of the mobile ion is then calculated using Eq. (4).

4. Results and Discussion

The details of the thermal behavior of system A as a function of GeO_2 content is presented in SI (see S1.1). The trend observed in the glass transition temperature, T_g, in system A (SI) and system B[44] as a function of relative GeO_2 content is taken up for discussion in the last section, in comparison with trends observed from electrical conductivity studies.

In this section, we first of all present the results on Raman spectra in a comparative manner for both system A: ($40Li_2O$-$(60-x)P_2O_5$-$xGeO_2$) and system B: ($40Li_2O$-$10B_2O_3$-$(50-x)P_2O_5$-$xGeO_2$), $0 \leq x \leq 25$ mol% and discuss them. This sets the tone for a detailed presentation and discussion of insights on structural units and cross linkages obtained via NMR. These are followed by results from analysis and modelling of conductivity and permittivity spectra to extract the spatial extent of localized diffusion.

4.1 Raman spectra of systems A and B

The evolution of the Raman spectra of system B as a function of germanate units was presented in Ref. 44. However, we present it alongside system A in Fig. 1, in order to clearly discern the influence of the borate units in system B, thereby comparing the role of four coordinated and six coordinated germanate units in the process of depolymerization of the phosphate network and find out changes in network structure in the two systems. In both systems, the Raman bands are assigned in accordance with literature data obtained for the previously studied germanophosphate glasses.[51-54]
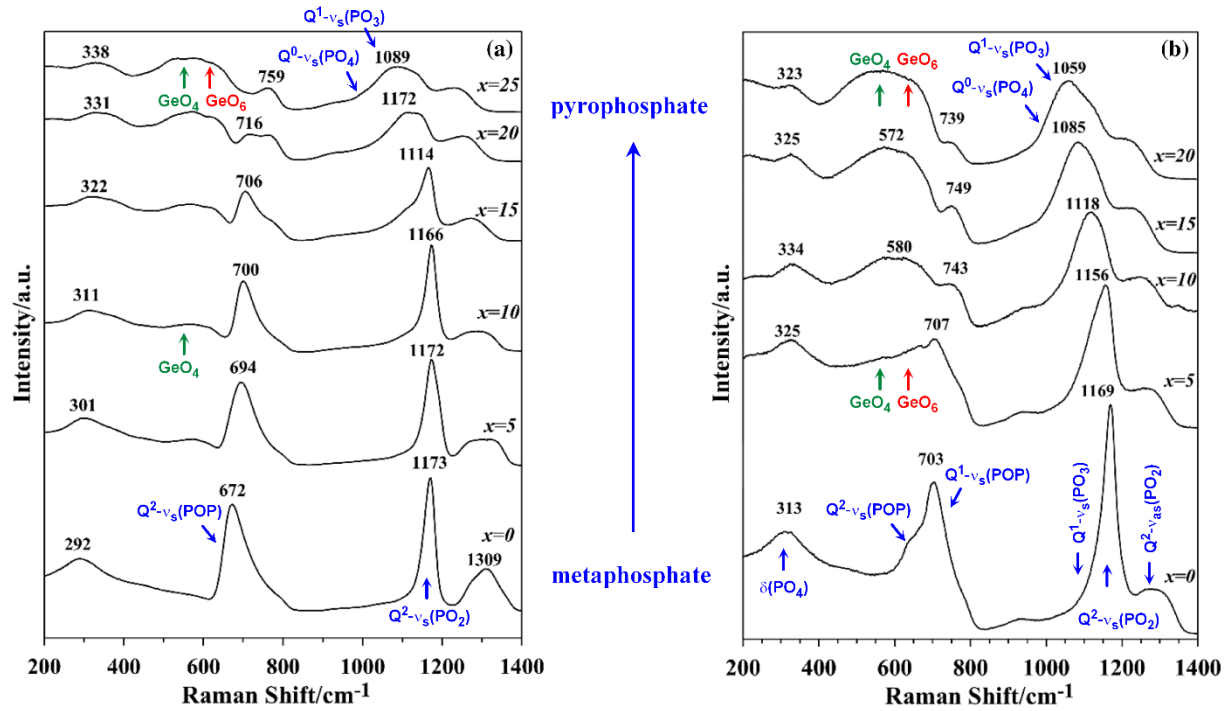
Figure 1. Evolution of Raman Spectra: (a) system A – ternary lithium germanophosphate glass and (b) system B – quaternary lithium boro-germano-phosphate glass[44], as a function of germanate content.

Comparing the x = 0 mol% for both systems, it is clear that the presence of 10 mol% borate, already has influence on the glass structure in that a) it depolymerizes the phosphate network, as is evidenced by the presence of symmetric stretching of pyrophosphate chains (Q^1 units) at around 703 and 1100 cm^{-1} and b) the intensity of the various bands, symmetric stretching $\nu_s(PO_2)$ of both Q^2 and Q^1 are higher. Also, note that the values of peaks for system A & B do not exactly match. This could be because of a great spectral overlap of the borate vibrational modes in system B. However due to low borate content, this cannot be resolved, and the spectral intensity is dominated by the phosphate structural units.[51]

For x > 0 mol%, the evolution of the spectra **in system A**, in contrast to system B, shows a good preservation of the peaks until x = 10 mol%. The main Raman band at 1172-1173 cm^{-1} ascribed to the symmetric stretching vibration of non-bridging oxygen atoms in Q^2 units[54] nearly does not change its position in the concentration range of x = 0 - 10 mol% GeO2, which corresponds to only small changes in phosphate structural units. Further, the emergence of the Ge^4 units at around 571 cm^{-1} units is barely discernible at x = 5 mol%, but becomes broader and clearer beyond x = 10 mol%. Beyond this, the P-O-P linkage represented by the peak at 672 cm^{-1} is replaced by broad shoulders and reduction of the peak, with broad bands between 550 and 650 cm^{-1}. This could imply formation of Ge-O-P linkages right from x = 5 mol%, however with progressive replacement of metaphosphate chains (Q^2 units) with pyrophosphate chains (Q^1 units). In a study on potassium germanophosphate glasses,[35] the authors recall that the signal at 531 cm^{-1} can be attributed to presence of three-membered rings[52] as seen in alkali germanate glasses with low alkali contents, and the signal at 650 cm^{-1} to the presence of vibrations associated with Ge^5 or Ge^6 units[55] in binary germanate glass. However, direct evidence from Raman spectra for this is weak.

In system B, already for x = 10 mol%, we see the signatures of bands corresponding to x = 25 mol% of system A. As mentioned earlier, the peaks are lightly different having been modified by the constant but low borate content. Hence, for x between 15 to 25 mol%, we observe in Fig. 1b, a significant increase in the broadness and intensity of the bands between 400 and 700 cm^{-1}. Since there is no way of resolving what exactly is responsible for this, at best we can conclude that cross bond linkages of Ge-O-P increases, as also an increase of NBOs since orthophosphate units are also present at x = 25 mol%. In short, in system B, the presence of low but constant borate content causes a strong modification of the phosphate network and increases the cross linkages of germanate units of both four- and higher coordination.

4.2 NMR studies on systems A and B

To start with, we present results from the ^{31}P MAS-NMR experiments obtained **on system A**, (40Li$_2$O-xGeO$_2$-(60-x)P$_2$O$_5$ glass series) in Fig. 2. Broad signals can be observed which are in good agreement with previous analysis of mixed network phosphate glasses.[15,18-20,25-26,40-41] As expected from the formulation, the binary composition (40Li$_2$O-60P$_2$O$_5$) presents two components (Fig. 2) at -40 and -26 ppm that can be assigned to Q^3 and Q^2 sites, respectively. The relative proportions deduced from the decomposition (Table 2) are in good agreement with the values calculated from the O/P ratio, confirming our assignments.
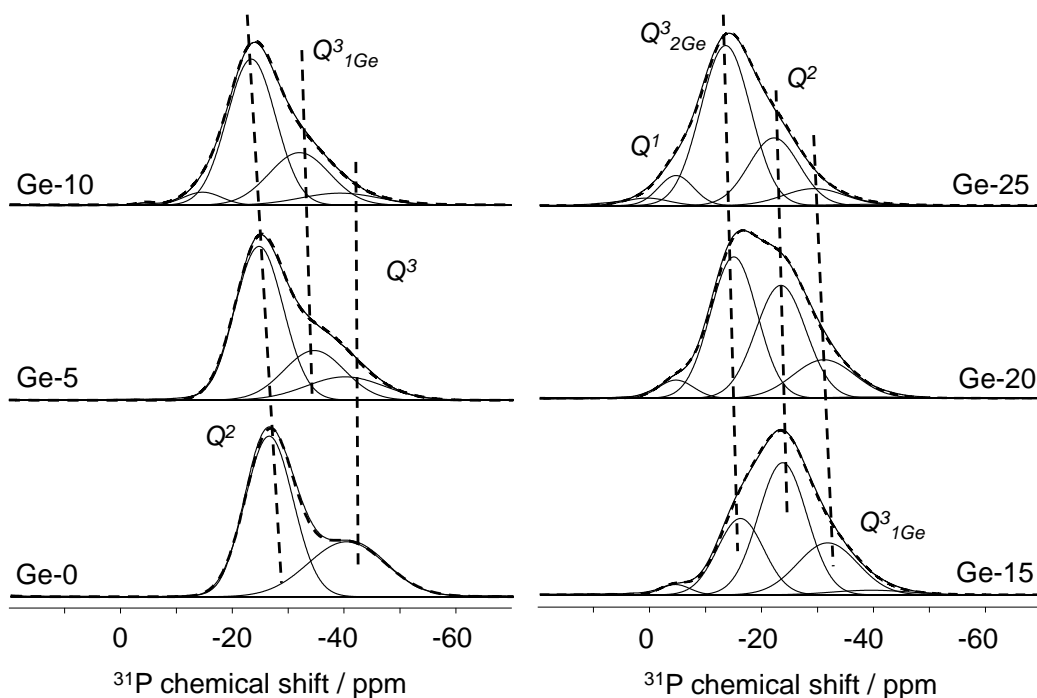

Figure 2. ^{31}P MAS-NMR experiments performed on system A, the 40Li$_2$O-xGeO$_2$-(60-x)P$_2$O$_5$ glass system. The spectra are accompanied by the decompositions performed with the dmfit software.[20]

17

Table 2. ^{31}P NMR parameters obtained with a Gaussian model. Chemical shifts (δ_{iso}), full width at half maximum (fwhm) and relative proportions (rel. prop.) are given with errors of +/- 0.2 ppm, 0.2 ppm and 2%, respectively.

GeO$_2$ / mol%	Q^n	δ_{iso} / ppm	fwhm / ppm	rel. prop. / %	GeO$_2$ / mol%	Q^n	δ_{iso} / ppm	fwhm / ppm	rel. prop. / %
0	Q^3	-40.1	16.3	33.0	15	Q^3	-39.3	16.5	3.0
	Q^2	-26.2	10.1	67.0		Q^2	-23.4	10.3	50.0
						Q^1	-4.5	6.2	1.0
5	Q^3	-39.9	16.3	14.0		Q$^3{}_{1Ge}$	-31.5	12.7	22.0
	Q^2	-24.6	10.1	64.0		Q$^3{}_{2Ge}$	-15.9	9.7	24.0
	Q$^3{}_{1Ge}$	-34.5	12.7	22.0	20	Q^3	-39.2	16.5	1.5
						Q^2	-23.1	10.5	36.5
10	Q^3	-39.2	16.5	7.0		Q^1	-4.4	7.3	3.5
	Q^2	-23.4	10.2	63.0		Q$^3{}_{1Ge}$	-30.8	12.9	15.0
	Q^1	-4.5	6.2	0.5		Q$^3{}_{2Ge}$	-14.7	9.8	43.5
	Q$^3{}_{1Ge}$	-32.0	12.7	26.5	25	Q^2	-21.9	10.5	25.0
	Q$^3{}_{2Ge}$	-14.6	8.1	3.0		Q^1	-4.4	7.3	8.0
						Q$^3{}_{1Ge}$	-29.1	10.5	8.0
						Q$^3{}_{2Ge}$	-13.3	10.5	57.0
						Q$^3{}_{3Ge}$	0.8	9.18	2.0

When GeO$_2$ is introduced into the formulation, this two components model does not permit an efficient decomposition, indicating that the phosphate network has been significantly modified. Suitable decompositions require the addition of a third component at -34.5 ppm that is thus assigned to a P connected to Ge^{4+} ions. At x = 10, a fourth signal appears at -14 ppm that can also

be assigned to a second phosphate site connected to Ge^{4+} ions. Finally, at high GeO_2 contents, this species becomes the dominant signal and two low intensity signals appear at -4 and 1 ppm. The first site can be assigned to Q^1 species from previous investigations on the Li_2O-P_2O_5 system and the site at 1 ppm has to be attributed to a third phosphate species connected to Ge^{4+} ions. These results are visually reported in Fig. 3a by presenting evolution of relative proportion of each phosphate species. At low GeO_2 content ($0 < x < 10$), the Q^3 species are significantly consumed to create the first mixed units (at -34.5 ppm). Therefore, it can be reasonable admitted that this site is created through the reactivity between Q^3 and Ge^{4+} according to the following mechanism:

$$2 Q^3 + GeO_2 \rightarrow 2 Q^3_{1Ge}$$
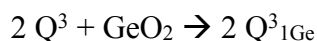
In the notation Q^3_{1Ge}, the superscript 3 refers to the 3 bridging oxygens 1 of which links to Ge^{4+} ion and (3-1) of which link to P^{5+} ions. Note that the corresponding phosphate species is metaphosphate. Thus, this mechanism shows that while the phosphate network depolymerizes, the global glass network reticulation increases.

It is noteworthy that the chemical shift values of this site (-34.5 ppm) lie between the values of Q^3 (-40 ppm) and Q^2 (-26 ppm), which also supports our assignment. At higher GeO_2 contents (10 $< x < 20$), the Q^2 and Q^3_{1Ge} species decrease in favor of the second mixed species (-14 ppm). We believe that this site is a Q^3_{2Ge} species created through the reactivity between one Ge^{4+} ion and Q^3_{1Ge} but also from reactivity between two Ge^{4+} ions and Q^2 sites. Only a slight modification of the phosphate network can be observed at x = 25, with the appearance of a third mixed species assigned to Q^3_{3Ge} units accompanied by Q^1 moieties.
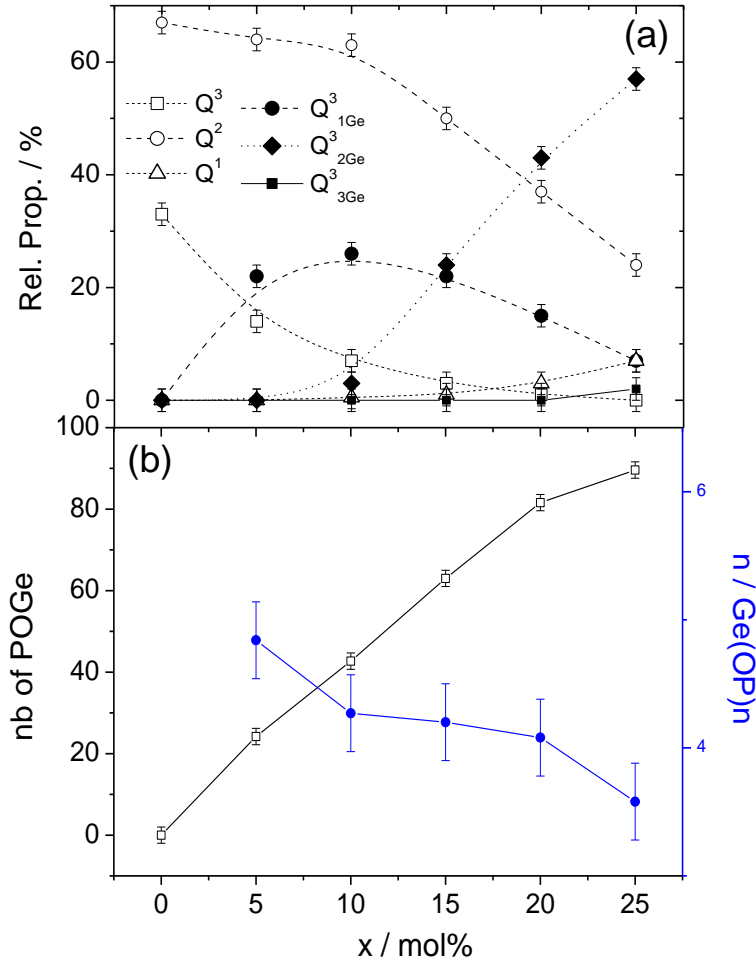
Figure 3. (a) Evolution of the Q^n relative proportions deduced from the 31P MAS-NMR experiments decomposition; (b) Number of POGe deduced from the 31P NMR experiments (open squares) and number of P connected to Ge ions.

Two structural parameters were calculated from the ^{31}P MAS-NMR spectra decomposition. First, the total number of POGe linkages was obtained from the relative proportion of each phosphate species and the number of Ge attached to each phosphate species (m in the Q^n_{mGe} notation). The results are reported in Fig. 3b as open squares, which shows a continuous increase of the POGe bonds with the GeO_2 content. This results indicate that the glass network adopt a

mixed character without any segregation between the phosphate and the germanate networks. The second structural parameter that can be retrieved from the data of Tab. 2 is the number of P attached to each Ge^{4+} ions. These data are obtained for each glass by dividing the number of GeOP bonds in the network (equal to the number of POGe bonds previously calculated) by the number of Ge^{4+} ions in the formulation and are reported in Fig. 3b as full circles. This number, denoted as n in the $Ge(OP)n$ notation, is equal to 4.8 in the x = 5 glass and decreases with the GeO_2 content down to 3.86 in the x = 25 sample. Moreover, if we were to assume that no direct GeOGe bonding occurs in the investigated composition range and that Ge^{4+} ions are present under $Ge(OP)_n$ configuration, then n is directly related to the Ge coordination state. Therefore, Fig. 3b suggests that at low GeO_2 amounts, germanate is present as a mixture of four- and six-fold coordinated species with almost equivalent proportions or mainly under five-fold coordination state. This supports the findings from O K-edge XANES studies on alkali germanate glasses.[52] Evidence for the existence of five-coordinated state has also been obtained using neutron scattering measurements in cesium germanate glasses.[56,57] In the 10 - 20 mol% range, the six-coordinated species tend to decrease with the addition of GeO_2 to be replaced by $Ge(OP)_4$ species. At high GeO_2 content (< 20 mol%), the average number of P connected to Ge is lower than four, suggesting that Ge^{4+} ions are four-fold coordinated and that GeOGe bonds have been formed. Raman spectra for this system also support the idea of POGe cross linkages and show a continuous depolymerization of the phosphate network. However, more strong statements on the relative intensity of bands due to GeO_4 and GeO_6 units could not be made.

We now turn to results **for system B**. The 1D ^{11}B and ^{31}P MAS-NMR experiments performed on the $40Li_2O-10B_2O_3-(50-x)P_2O_5-xGeO_2$ composition line are presented in Figure 4, accompanied with representative decomposition of the ^{11}B NMR analyses (dotted lines). The [11]B

NMR experiments present well-separated regions for the B^3 (15/5 ppm) and B^4 (0/-10 ppm) units (Fig. 4a) allowing for a quick and efficient N^4 ($= B^4/(B^4 + B^3)$) determination but also for a detailed analysis of the borate speciation. The spectra show the presence of two tetra-coordinated species at -3 and -1 ppm and one tri-coordinated unit at 16 ppm. All the NMR parameters deduced from the decompositions are reported in Tab. 3.
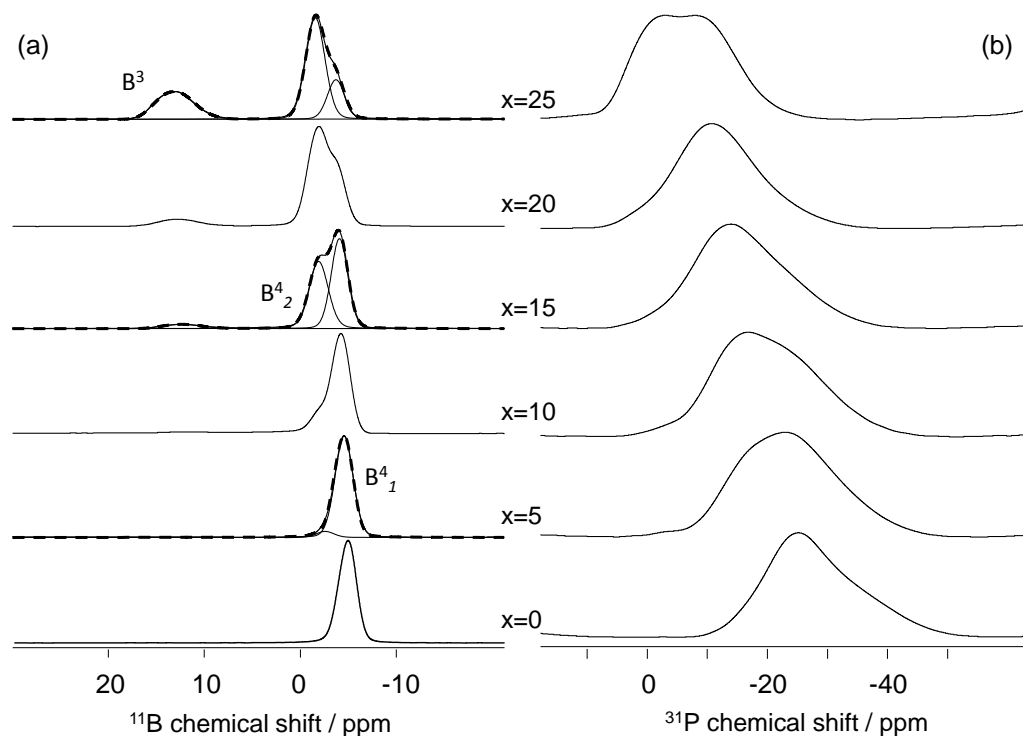

Figure 4. ^{11}B and ^{31}P MAS-NMR experiments performed on the 40Li$_2$O-xGeO$_2$-10B$_2$O$_3$-(60-x)P$_2$O$_5$ system. The ^{11}B NMR spectra are accompanied by representative decompositions showing the different borate species (dotted lines).

Table 3. ^{11}B NMR parameters. B^4 and B^3 units were simulated using the Gaussian and quadrupolar models, respectively. Chemical shifts (δ_{iso}), full width at half maximum (fwhm), relative proportions (rel. prop.), quadrupolar constant (C_Q), and asymmetry parameter (η_Q) are given with errors of +/- 0.2 ppm, 0.2 ppm, 1%, 0.1 MHz and 0.1, respectively.

x	B^4	δ_{iso} / ppm	fwhm / ppm	rel. prop. / %	B^3	δ_{iso} / ppm	C_Q / MHz	η_Q	rel. prop. / %
0	B^4_1	-3.9	2.1	100					
5	B^4_1	-3.7	2.2	95.0					
	B^4_2	-1.8	2.1	5.0					
10	B^4_1	-3.5	2.1	81.0	B^3_1	15.9	2.7	0.5	3.0
	B^4_2	-1.2	2.4	16.0					
15	B^4_1	-3.3	2.0	50.5	B^3_1	15.7	2.8	0.5	5.5
	B^4_2	-1.1	2.3	44.0					
20	B^4_1	-3.1	2.0	29.0	B^3_1	16.5	2.8	0.5	9.5
	B^4_2	-1.0	2.3	61.5					
25	B^4_1	-2.9	2.1	18.0	B^3_1	16.6	2.9	0.5	28.0
	B^4_2	-0.8	2.3	54.0					

The evolutions of N^4 and of the relative proportions of the three borate species are sketched in Fig. 5. As shown in Fig. 4a, insertion of GeO_2 tends to decrease the N^4 ratio by inducing the formation of B^3 units from the tetra-coordinated species present in the base composition. The obtained curves also show that the borate speciation is dominated at low GeO_2 content (10 < x < 20) by the B^4_1 units, this latter decreasing at higher x at the benefit of the B^4_2 species. Above 20 mol% of GeO_2, the borate speciation is modified by the replacement of the B^4_2 units by the trigonal B^3 species, although the borate network is always dominated by tetra-coordinated borate units. It

appeared thus crucial to determine the structural characteristic of the two B_4 units. In Li_2O-B_2O_3-P_2O_5 systems, B^4_1 site was assigned to B^4 attached to 4 tetrahedral species (P or B^4) whereas the second site B^4_2 was assigned to B^4 attached to at least one B^3 signal. Correlation NMR was applied to our system to confirm this assignment or to determine the effect of the GeO_2 insertion on the borate network organization.
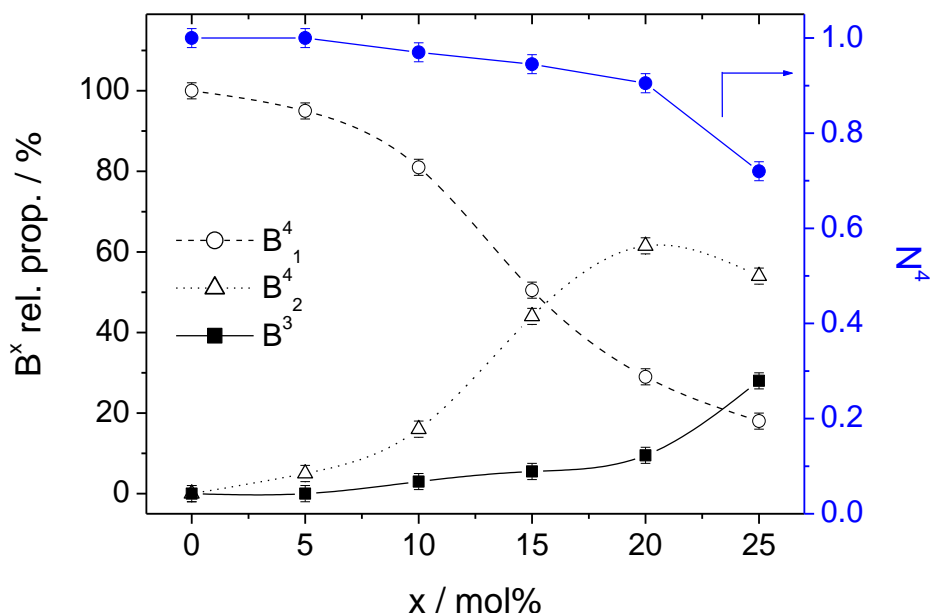

Figure 5. Evolution of the B^4_1, B^4_2 and B^3 borate species and of the N^4 ratio in the $40Li_2O$-$xGeO_2$-$10B_2O_3$-$(60-x)P_2O_5$ glass system.

Representative results about $^{11}B/^{11}B$ homonuclear NMR are displayed in Figs. 6a and 6b. Fig. 6a represents the 1D filtered ^{11}B spectra obtained with the ^{11}B DQSQ NMR experiment. This sequence was used to produce 1D ^{11}B NMR spectra only showing the borate species spatially close to other borate species, i.e. involved in BOB linkages. These ^{11}B filtered NMR analyses (Fig. 6a) for the x = 0, 5, 20 and 25 samples) present a poor signal to noise ratio suggesting that the number of borate involved in BOB linkage is low. At low GeO_2 content, low intensity signal showing interaction between B^4_1 units can be observed in a good agreement with the $B(OX)_4$ (X = P, B^4)

assignment. At $x = 20$, the filtered spectrum shows that both B^4_2 and B^3 participate in the formation of BOB bonds. While the 1D spectra support the previous assignment of B^4_2 to $B(OX)_{4-n}(OB^3)_n$, the 2D map afford original insight. Indeed, while the 2D was supposed to confirm the presence of B^4-O-B^3 bonds through the appearance of off-diagonal signal between these two sites, only on-diagonal signal involving B^4 and B^3 units can be observed. This unexpected result indicates that no B^4-O-B^3 bonds exist in the glass network and that the assignment determined for Li_2O-B_2O_3-P_2O_5 system is not suitable in our compositions. Insertion of GeO_2 significantly alters the borophosphate network by suppressing the B^4-O-B^3 connectivity. We propose that the environment of the second B^4 site is modified in this system by Ge^{4+} ions (and not B^3 as in previous system) leading to a $B(OX^4)_{4-n}(OGe)_n$ assignment.
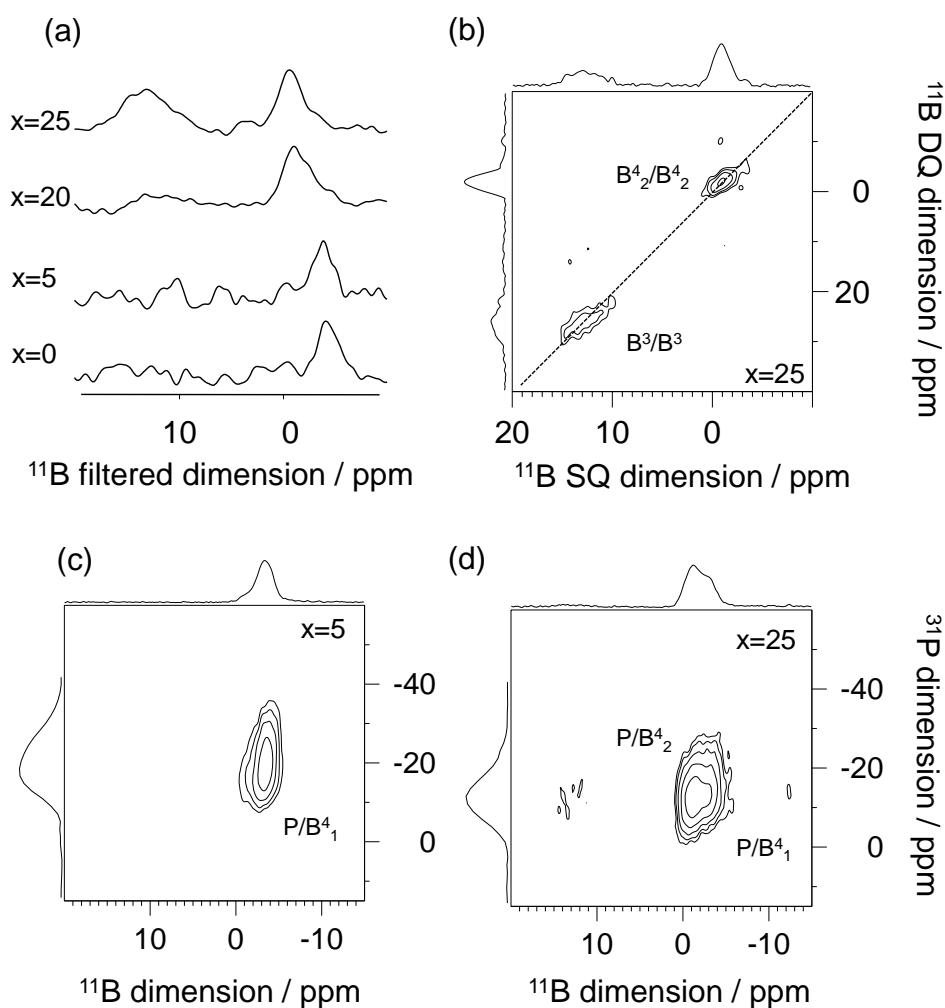
Figure 6. Correlation NMR results: (a-b) $^{11}B/^{11}B$ homo-nuclear correlation NMR: 1D filtered ^{11}B NMR spectrum (a), 2D $^{11}B/^{11}B$ correlation map obtained on the x = 25 sample (b). (c-d) $^{11}B/^{31}P$ hetero-nuclear correlation NMR: 2D $^{11}B/^{31}P$ maps obtained on the x = 5 (c) and 25 (d) samples.

Now we can turn our attention to the phosphate first analyzed by 1D NMR technique. The spectra, reported in Fig. 4b, are composed by very broad and uninformative resonances, resulting from the superimposition of several signals as already observed in various borophosphate systems[15,18-20]. Only a global shift towards positive chemical shift values can be observed when GeO$_2$ is introduced in the formulation, indicating an overall depolymerization of the phosphate

network. Deeper analysis of the ^{31}P MAS-NMR experiments is permitted by the edition of 2D $^{11}B/^{31}P$ correlation maps. The 2D maps recorded on the x = 5, and 25 are reported in Fig. 6c and 6d, and the other 2D maps are presented in SI (see S2). The 2D maps are accompanied by the ^{11}B and ^{31}P 2D projections in the horizontal and vertical axes, respectively, that represent the borate and phosphate species involved in POB linkages. The 2D maps show a first type of POB bonds involving the B^4_1 units at low GeO_2 content. This latter is then accompanied by a second linkage between the B^4_2 and phosphate units. It is noteworthy that the ^{31}P projections displayed with the 2D maps gather the phosphate units connected to these two different borate species under a single component in order to avoid any over-interpretation. A detailed analysis of the 1D ^{31}P MAS-NMR spectra using the ^{31}P projections of the 2D maps as input parameters is described and presented in SI (see S2). The results show that the phosphate and borophosphate networks are strongly impacted by the insertion of Ge atoms. Presence of phosphate species connected to borate only, to borate and germanate and of phosphate connected to germanate atoms is determined. Altogether, the network appears to be composed by at least six different phosphate species. While the results confirm that the three former element mix together, attempt at a more complete description fails due to the lack of information about the number of connected Ge^{4+} ions, rendering thus the description of the phosphate network only qualitative. However, unexpected results are provided by our 2D NMR analysis. Indeed, no interaction between B^3 and P is highlighted by our experiments even at high GeO_2 content where the proportion of B^3 reaches 30%. Here again, a major difference is observed between our system and standard borophosphate network where B^3 sites do mix with phosphate to create bonds. Insertion of GeO_2 does not allow for the creation of these mixed linkages and since B^3 is only connected to other B^3 units (Fig. 6b), it turns out that the global network presents a significant degree of inhomogeneity with the mixing together of B^4, P

and Ge separated from tri-coordinated boron that are only attached to other B^3 units and probably Ge atoms.

4.3 Conductivity spectra of systems A and B

Fig. 7a shows the frequency dependence of the ionic conductivity at different temperatures for system A with 15% GeO_2 content. Typically, each isotherm in ionic glasses exhibits two features of interest for understanding the ion dynamics: a plateau (DC conductivity) at lower frequencies and dispersion at higher frequencies. The DC-conductivity is related to diffusive or translational motion of the ions, and is hence activated, showing an Arrhenius behavior (cf. Fig. S3 in SI). The dispersive behavior is attributed to correlated forward-backward ion hops and is more visible at lower frequencies at lower temperatures, and shifts to higher frequencies at higher temperatures. In addition, at higher temperatures, in the low-frequency side electrode polarization effects are visible due to the accumulation of mobile ions near the blocking metallic electrodes. In system A, it is seen from Fig. 7a that in the frequency range covered by impedance spectroscopy for the isotherm at 213 K and below DC conductivity is not yet attained, while above 363 K there is no dispersive behavior observed. The permittivity spectra are displayed in the Fig. 7b for the same temperature range. We see that at higher frequencies, the real part of the permittivity tends to a constant value, $\varepsilon(\infty)$, which results from rapid polarization processes occurring in the glasses under an applied field. With decreasing frequency, however, the real part of the permittivity increases and approaches a limiting low-frequency plateau, ε_s, denoted as the low-frequency static value which is associated with the polarization effects of the ions with respect to the immobile glass matrix. It is not always easy to determine the dielectric strength of relaxation, $\Delta\varepsilon = \varepsilon_S - \varepsilon(\infty)$, in

ionic glasses, due to the effect of electrode polarization effects, visible as a steep increase in the permittivity values, which are indicated in Fig. 7.
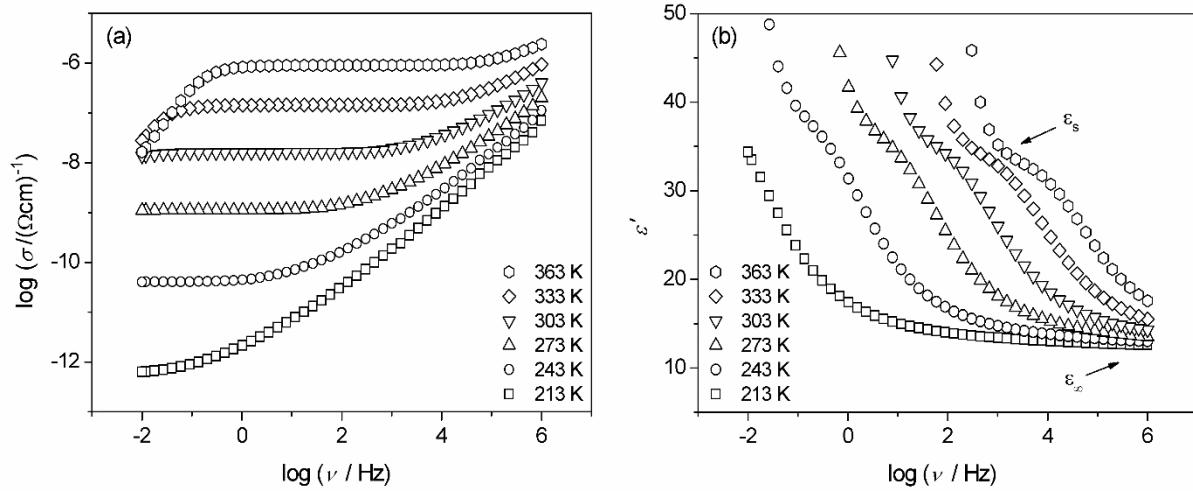

Figure 7. Conductivity (a) and permittivity spectra (b) as a function of temperature for the Ge-15 glass (system A) measured at different temperatures. See Ref. 44 for similar spectra for system B.

After removing the contributions of electrode polarization effects, the isotherms for the various glass compositions can be scaled using the relations given in Eqs. (1) & (2). Scaled conductivity and permittivity spectra are shown for system B with 10 mol% GeO_2 in Fig. 8. It is found that for all glass compositions studied here, the model spectrum with shape parameter $K = 2.0$ reproduces best the form and shape of the experimental conductivity isotherms as shown in Fig. 8a. This value for the parameter K is typical for many single-alkali ion conducting glasses[45,48] with medium alkali oxide content and containing oxides such as borate, germanate or phosphate. This result confirms results of previous work on sodium borophosphate glasses.[17] Further, it is found that the logarithm of the frequency of onset of conductivity dispersion, $\log(\nu_0)$ determined for each isotherm by shifting the experimental conductivity isotherm, $\log(\sigma(\nu)/\sigma_{DC})$ on to the model curve, lies on a line of slope one.
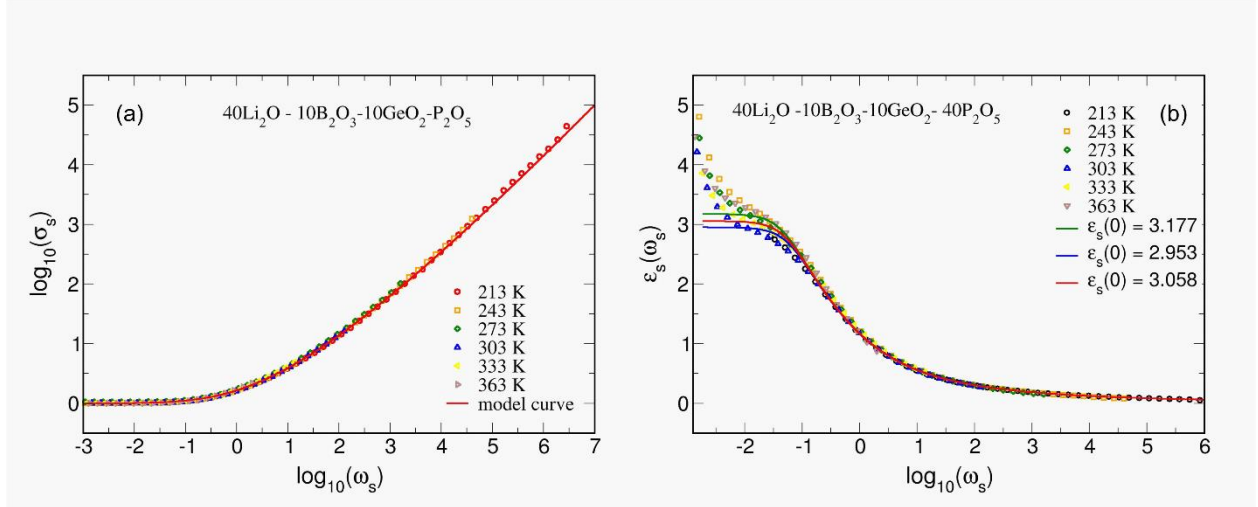
Figure 8. Scaled experimental conductivity (a) and permittivity (b) spectra superimposed on corresponding model curves with $B = 25$, $K = 2$. In the right hand panel, the $\varepsilon_S(0)$ plateau values are obtained by using $N(\infty) = 0.08 \pm 0.01$.

Fig. 8 also shows model curves for the scaled conductivity and permittivity spectra. Displayed in the Fig. 8b are three model curves for different value of the parameter for the value of $N(\infty)$ due to the spread in the value of the experimental scaled permittivity plateau, $\varepsilon_S(0)$. As shown in Appendix B (left panel of Fig. A2 in *Parameters of the Model*), the value of $N(\infty)$ affects the height where the scaled permittivity plateau is reached. This helps in estimating the uncertainty in accurate determination of the plateau. This error for all glass compositions in both systems studied lies in the range of 4-7%.

Using the values for $\varepsilon_S(0)$ for each isotherm, using Eq. 4 the value of $< r_{loc}^2(\infty) >$ and its square root is estimated, which as expected turns out to be a constant for each composition. The error range of this value is about 2-4%, reflecting the error in $\varepsilon_S(0)$. As explained in Appendix A, Sidebottom and co-workers[58] calculated a characteristic length, L, as typical length-scale for diffusive motion, using the simple Nernst-Einstein relation between DC-conductivity, σ_{DC}, and

diffusion coefficient, D, from the equation: $L^2 = \frac{6k_B}{N_V q^2} \cdot \frac{\sigma_{DC}T}{(\omega_O/2\pi)}$. See Appendix A for details. For

calculating either L or $< r_{loc}^2(\infty) >^{0.5}$, the number density of mobile ions, N_V, is needed. This is

calculated for all compositions of system A using details on density and volume given in Table 1.

For system B, these details are available in Ref. 44. Note, however that the density of the glass

composition corresponding to 25 mol% GeO2 content for system B is unavailable.

   In order to understand the localized and diffusive ion dynamics as a function of germanate

content, various quantities of interest are plotted in four panels of Fig. 9 for both systems (see the

tables in S3 of SI). All quantities that are plotted are temperature-independent. The bottom panel

shows the variation of N_V and the topmost panel the variation of the spatial extent of the localized

diffusion, $< r_{loc}^2(\infty) >^{0.5}$. In the second panel from the bottom the factor $\frac{\sigma_{DC}T}{\omega_O}$ is plotted, which is

proportional to the product $N_V \cdot L^2$. Recall from Eq. (2) (cf. Sec. 3) that $\varepsilon_S(0)$ plotted in the third

panel from bottom is a product of $\omega_O \cdot (\varepsilon_0 \Delta\varepsilon/\sigma_{DC})$, which is the scaled Sidebottom time, $t_{SB,S}$.[6,17,45]

Note that, since $\varepsilon_S(0)$ is scaled by the angular frequency at the onset of conductivity dispersion, it

is proportional to $\Delta\varepsilon \cdot T$ and is a temperature-independent material property for systems that obey
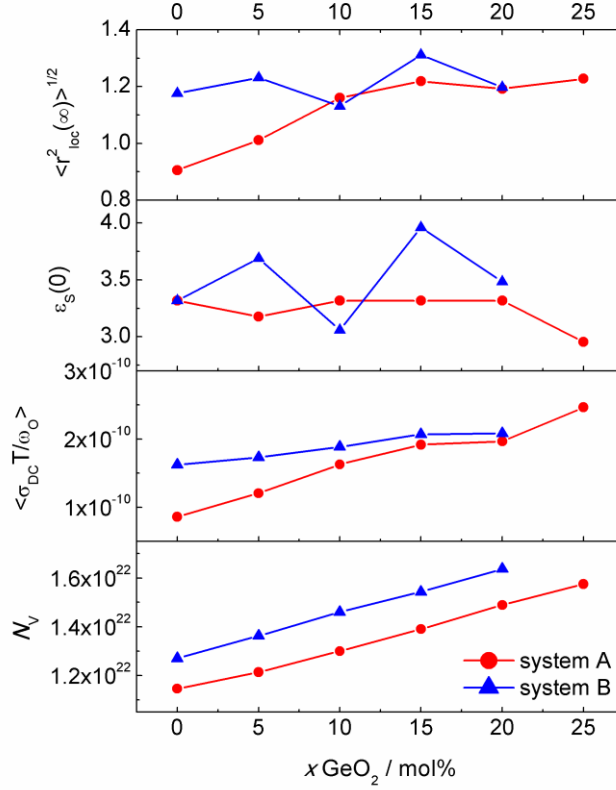
Summerfield scaling.[49]

Figure 9. Plots of various material-dependent properties as a function of the relative germanate content for system A (lithium germanophosphate glass) and B (lithium boro-germanophosphate glass). See text for details. Note: the units of N_V is cm^{-3}, that of $< \sigma_{CB} T / \omega_O >$ is Scm^{-1}Ks and $< r_{loc}^2(\infty) >^{0.5}$ is Å, while $\varepsilon_S(0)$ is dimensionless.

First, we consider **system A**. We observe from Fig. 9 that N_V shows a near linear increase; the second panel which is equivalent to the product $N_V \cdot L^2$ shows a linear increase until x = 15 mol%, a levelling off at x = 20 mol%, and then again an increase for x = 25 mol%; the value of $\varepsilon_S(0)$ remains nearly a constant decreasing a little from that for the binary composition, and decreases further for x = 25 mol%. Each of these three factors enter the calculation of $< r_{loc}^2(\infty) >^{0.5}$ (refer to Eq. (4)) and one observes that the trend shown by it is similar to that exhibited by $N_V \cdot L^2$ except for x = 25 mol%. Its value increase from about 0.9 to 1.2 Å.

Now moving on to **system B**, which is ternary for x = 0, and quaternary for x > 0, we observe interesting features. A general point is that N_V is higher for these glasses in comparison to system A. This could mean a more compact network, and could result in smaller values of $< r_{loc}^2(\infty) >^{0.5}$, see Eq. (4), if all other factors were similar to that of system A. However, we observe from Fig. 9. that N_V shows a near linear increase; the product $N_V \cdot L^2$ remains nearly a constant increasing a little until x = 15 mol%, a levelling off at x = 20 mol%. On the other hand, the value of $\varepsilon_S(0)$ varies alternately up and down for each increase of the germanate content between 3.0 and 4.0. Here the trend shown by $< r_{loc}^2(\infty) >^{0.5}$ is found to be similar to that exhibited by $\varepsilon_S(0)$, modulated down in magnitude, varying between 1.2 and 1.3 Å.

In Fig. 10. we plot the two length scales of ion dynamics, one pertaining to localized diffusion, $< r_{loc}^2(\infty) >^{0.5}$, and Sidebottom length L, which is a characteristic length of diffusive motion. Before we can interpret the results, following aspect is important to be borne in mind. Although these are two different length scales, a detailed analysis has shown that in glassy materials where polarizabilities do not play a major role, the two are proportional.[16,17,59] On a perusal of Fig. 10, where the two length scales are plotted versus charge carrier number density, following features can be clearly discerned: (i) in system A, both $< r_{loc}^2(\infty) >^{0.5}$ and L exhibit similar trends although the magnitudes are different; (ii) in system B, the effect of low but constant borate content results in a near constant value for L and a fairly constant but mildly fluctuating values of $< r_{loc}^2(\infty) >^{0.5}$ indicating that increase of germanate content has less influence on diffusive ion dynamics. These and other aspects will be considered in the next section.
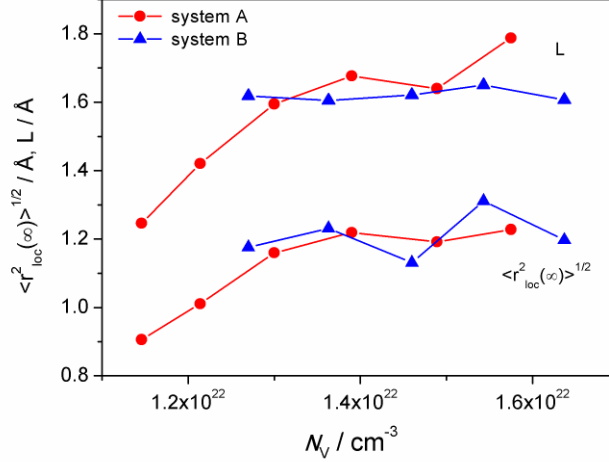
Figure 10. Comparison of spatial length of localized diffusion and Sidebottom length as a function of number density of mobile ions for systems A & B. Note that increasing N_V corresponds to increasing mol% of GeO_2 from 0 to 25.

5. Correlations between local structure and localized and diffusive ion dynamics

We now proceed to consider our results on length scales from insights gathered from local structure. Here we start with system A, and by considering our results in relation with that obtained in literature for other systems. It is seen from Fig. 9, that the value of $< r^2_{loc}(\infty) >^{0.5}$ in the binary system $40Li_2O\text{-}60P_2O_5$ (x = 0 mol%, system A) is about 0.9 Å. This value is larger than the value of 0.73 Å obtained in sodium borophosphate.[16,17] In their glass, as in our binary glass here, structural studies show that metaphosphates to ultraphosphates is in ratio 2:1 (see Table 2, and Ref. 15). However, at room temperature, σ_{DC} of $40Li_2O\text{-}60P_2O_5$ is about five times larger than that of $40Na_2O\text{-}60P_2O_5$ at room temperature. While a larger value of $< r^2_{loc}(\infty) >^{0.5}$ can imply that the potential wells for the mobile ions are shallower,[17] possibly the smaller size of the cation plays an additional role in aiding its mobility. *Thus, given a similar network connectivity, a larger value of rms of localized diffusion seems to be directly correlated with higher conductivity.*

Further, an increase in $< r^2_{loc}(\infty) >^{0.5}$ for our system A, i.e., $40Li_2O$-$(60-x)P_2O_5$-$xGeO_2$ from 0.91 to 1.16 Å already happens when x changes from 0 to 10, and increases to 1.23 Å for x = 25 mol%. A similar increase from 0.73 to about 1.0 Å is seen in $40Na_2O$-$60[x(B_2O_3)$-$(1-x)(P_2O_5)]$,[16,17] for the characteristic length-scale of hopping, as x increases from 0 to 0.4, implying B_2O_3 content increases from 0 to 24 mol%.[16] In borophosphate systems, with either sodium or lithium as the mobile ion, the MGFE is caused by the increase in anionic B^4 units as a function of increasing borate content,[16] and also due to increase in cross linkages of the pyrophosphate with the B^4 units.[20]

However, both from Raman spectra and ^{31}P MAS-NMR studies (Figs. 2, 3 and Table 2) we see that the phosphate network breaks up and the cross-linkages POGe increases continuously. The trend shown by open squares in Fig. 3b matches those shown by the second and fourth panel for system A in Fig. 9, signaling that increased network connectivity provides shallower potential wells[17] and a steady increase in the spatial extent of localized diffusion. The trend shown by decrease of n, that the number of Ge attached to each P ion decreases (blue triangles of Fig. 3b) provides only an indirect evidence of Ge/Ge mixing, which is also similar to the trend displayed by $\varepsilon_S(0)$ for system A (the third panel from bottom in Fig. 9).

Another aspect that we observe from NMR results (Table 2, Fig 3), is that although the cross linkages of P-O-Ge is modest (Q^3_{1Ge}) up to 10 mol% GeO_2 content, it produces a steeper increase in DC conductivity, T_g and $< r^2_{loc}(\infty) >^{0.5}$. From 15 mol% GeO_2 content, the growth of cross linkages (Q^3_{2Ge}) increases strongly. However, this might also be the regime where GeOGe bonds might start to compete with POGe linkages, resulting in a weaker increase in the three quantities. At 25 mol% content, we have about 60% mixed species of Q^3_{2Ge} type, together with inhomogeneous GeOGe linkages and hence isolated and non-homogeneous germanate units (also

indicated in Fig. 1), which might also provide additional basins for the Li^+ ion, causing an enhancement in the ease of ion transport - localized or diffusive.

Let us now consider Fig. 11. The similarity in the behavior of T_g and σ_{DC} has been discussed and is recognized as a typical signature of alkali containing MGF glasses.[15,17,20,23] In borophosphate glasses, it has been attributed to depolymerization of phosphate network, accompanied by increased network connectivity that facilitates ion transport due to formation of tetrahedrally coordinated borate units.[15-17,20] What is remarkable in system A is that the non-linear increase is steeper in T_g and σ_{DC}. For example as x goes from 0 to 20 mol%, system A shows an increase of about 200 K in T_g and a four orders of magnitude increase in σ_{DC} and a 30% increase in the value of $< r_{loc}^2(\infty) >^{0.5}$. In this same range of x, system B shows an increase of about 100 K in T_g and about two orders of magnitude increase in σ_{DC}, and a narrow range but fairly remarkable variation in $< r_{loc}^2(\infty) >^{0.5}$.
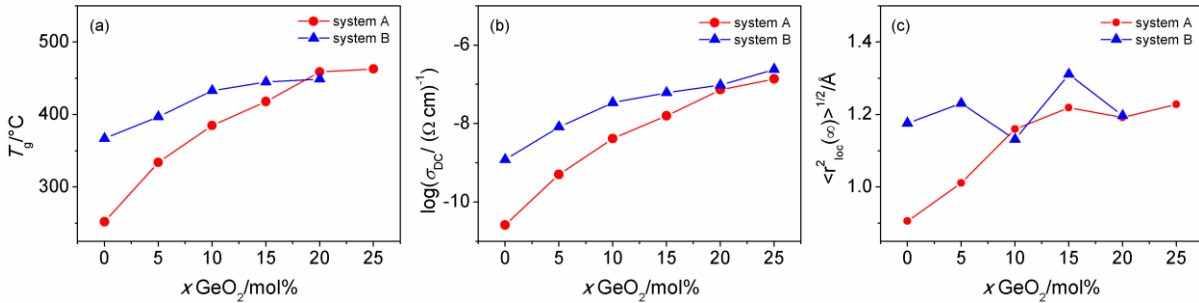

Figure 11. (a) variation of glass transition temperature, T_g; (b) variation of DC conductivity, σ_{DC} at 303 K and (c) variation of spatial extent of localized diffusion as a function of germanate content for system A (red circles) and system B (blue triangles), same as in Fig. 9.

Using Fig. 11, and moving on to system B, we consider the *ternary* glass (0 mol% GeO_2) and make a comparison to similar composition in the Zielniok sodium borophosphate glass: $40Na_2O$-

$6B_2O_3$-$54P_2O$.[16,17] Their values of σ_{DC} at 298 K is about two orders of magnitude smaller and $< r^2_{loc}(\infty) >^{0.5}$ is also smaller than that for our ternary composition of system B. These result again point to the possibility that the smaller Li^+ ion is more loosely bound to its immediate neighboring network former units, despite a more compact network, which makes its local excursions larger and diffusion higher.

Further, when one considers the two glasses, $40Li_2O$-$10B_2O_3$-$50P_2O_5$ and $40Li_2O$-$10GeO_2$-$50P_2O_5$ one sees that at 303 K, σ_{DC} of the borophosphate glass is 1.2×10^{-9} Scm^{-1} and is comparable to that of the ternary germanophosphate glass whose σ_{DC} is 4.16×10^{-9} Scm^{-1}. Even the values of $\varepsilon_S(0)$ and that of $< r^2_{loc}(\infty) >^{0.5}$ within the error margins are nearly identical! However, although we see a same steep increase in the spatial extent of localized diffusion going from pure lithium phosphate glasses to 10 mol% of either germanophosphate or borophosphate glasses, which may be attributed to the depolymerization of the phosphate network, the actual structural influences are somewhat different. What is common is that the phosphate network is depolymerized and either B-O-P[16,20] or Ge-O-P cross linkages are formed (Fig. 3b and Table 2). *For long-time dynamics, the enhanced network connectivity seems more important than the actual structural units.*

When we move onto quaternary system B and consider the effects as x increases, there are two main changes in network connectivity inferred from the novel NMR techniques. Firstly, at x = 10 mol%, a new phosphate species appears (around -25 ppm) that is connected to B and also probably to Ge (cf. Tab. 1 in SI). However, from x = 15 mol% B^3 units increases but these are not connected to phosphate units. This implies that only B^3/B^3 and B/Ge connectivity can occur. Further, because all the polyhedral formed do not mix, one can infer that the network is not homogeneous. A decline in network connectivity can then explain why for x > 10 mol%, both T_g and DC conductivity increase rather slowly (see Fig. 11). Since the mobility or diffusive dynamics of the lithium ions

decline, the value of $\varepsilon_s(0)$ and $< r^2_{loc}(\infty) >^{0.5}$ mirror the local excursions which fluctuate due to change in the structural units that act more like Coulomb traps rather than as doorway for the diffusion of the cations. However, surprisingly, L remains a constant. Two effects are hard to distinguish from NMR or from our calculation. While tetrahedral borate ions provide NBOs and hence shallower potential wells for making ions linger around the dispersed negative charges, and hence larger values of $< r^2_{loc}(\infty) >^{0.5}$, B^3 units not bonded to P_2O_5 or GeO_2 can provide a doorway effect,[17] allowing for faster ion diffusion. Thus, depending on where the mobile cation finds itself, the two competing effects come into play. One sees from Fig. 11 that for system B and system A, at x = 25 mol% σ_{DC} increases. This may have very well to do with ion motion facilitated by such doorway effects around a B^3-O-Ge or B^3-O-P linkages in system B and due to Ge/Ge mixing.

6. Conclusions

This study has addressed the changes to local structure in a ternary and quaternary mixed glass former system where lithium ion is the mobile species. Main general inferences are a) continued depolymerization of the phosphate network is one major tunable component for enhancing conductivity in MGF systems; b) novel NMR techniques allow us to gleam into local structures even in quaternary systems, and c) MIGRATION concept allows us to estimate local excursions of ions and thereby understand the diffusive dynamics.

In the ternary lithium germano-phosphate glass, using the ^{31}P NMR MAS experiments, the continuous modification of the network could be quantified over the entire range of glass composition studied. Thus, starting from just the ultraphosphate and metaphosphate units at x = 0, we observe five species of phosphate units at x = 25 mol% - three of them with P-O-Ge linkages, and notably, no ultraphosphate units survive. There is some indirect evidence of Ge/Ge mixing, but no quantification was possible.

For the quaternary system, the 1D ^{11}B MAS NMR provides a clear quantification of the borate units as GeO_2 is incorporated into the system. The tetrahedral borate units are replaced by trigonal units from x = 15 mol%, and at x = 25 mol% there are up to 30 % trigonal borate units. Further, when this is probed with ^{11}B/^{11}B homonuclear NMR as well as by 2D correlation maps show that a) B-O-B mixing is low: b) insertion of GeO_2 significantly alters the borophosphate network by suppressing the B^4-O-B^3 connectivity and c) P-O-B^4 dominates, and no P-O-B^3 linkages are visible even for 25 mol% GeO_2. These analysis help understand the ^{31}P MAS-NMR experiments, which only showed very broad and uninformative resonances indicating an overall depolymerization of the phosphate network. Thus, insertion of GeO_2 in lithium borophosphate network results in at least six different phosphate species, and only three of them mix. Thus it turns out that the global network presents a significant degree of inhomogeneity with B^4, P and Ge mixing together separated from tri-coordinated boron that are only attached to other B^3 units and probably Ge atoms.

Based on our model analysis of the conductivity and permittivity spectra, length scales for localized diffusion are extracted and were examined as a function of germanate content and number density of mobile ions. Another quantity, called the characteristic length, L, related to the diffusive dynamics[56] was also estimated for both systems. Correlating the information based on local structure and estimates of the local excursions of the lithium ion, the main findings are that in the ternary system (system A), the localized diffusion of the lithium ion is facilitated by the continuous modification of the phosphate network and formation of mixed species between phosphate and germanate. Thus, increased network connectivity provides shallower potential wells and a steady increase in the spatial extent of localized diffusion. However, in the quaternary system (system B), the presence of borate content as low as 10 mol% results in the depolymerization of

the phosphate network with cross linkages to the B^4 units, and addition of GeO_2 causes additional structural units and cross-linkages, while network connectivity seems probably affected. Although quantification of these is not possible, one can infer this from a slower increase of mobility and conductivity. Thus, while in system A, the similarity in trend of the product $N_V \cdot L^2$ to the trend exhibited by conductivity implies that the local ion excursions are well correlated to change in local structure resulting in a near constant value for the scaled permittivity plateau, $\varepsilon_S(0)$, across the range of variation in germanate content. Hence, the spatial extent of localized diffusion seems to reflect the ease of the mobility of the Li^+ ions. In contrast for system B, model analysis shows that the trend of the product $N_V \cdot L^2$ is much flatter in comparison to system A, implying that the local excursions are dominated by fluctuating values of $\varepsilon_S(0)$ over the studied composition range. This seems to imply that the Li^+ ion encounters more traps, which provides an explanation as to why the increase in DC conductivity with increasing GeO_2 content is slow, and also why it shows a limited increase in comparison with system A.

Appendix A　　　　　　　<u>A Note on Relevant Length Scales</u>

Length scales of ion transport in oxide-based glasses if they reflected typical anion-anion separation distance assuming that Coulomb interactions dominate could be of the order of 4 Å. Sidebottom[58] defined L as a characteristic hopping length for the mobile ion which is a temperature-independent quantity: $L^2 = \frac{6k_B}{N_V q^2} \cdot \frac{\sigma_{DC}T}{(\omega_O/2\pi)}$. This definition uses the well-known Nernst Einstein relation which links ionic conductivity to diffusion. It also assumes that the experimental frequency corresponding to the onset of conductivity dispersion, i.e. $\nu_O = \omega_O/2\pi$ at $\sigma = 2\sigma_{DC}$ is a good measure of DC hopping rate for the ion.

For various glasses with > 30 mol% alkali ion concentration, L was found to be typically of the order of about 1 Å, while this value increases to about 4 Å for very low alkali ion concentration: L = R/3 & R = $N_V^{-1/3}$, where R is anion-anion separation. Although this result was initially surprising, given that P-O distance is 1.55 Å, O-O distance is 2.51 Å and NBO distance is about 4 Å (from neutron scattering).

The authors argued[58] that if one were to include contributions of the slower ions, the average hopping rate could be set at $\nu_O/10$, then L would be larger by a factor of 3.16, and is then more comparable to length scales in the glass host. However, they inferred that "this small hopping distance clearly indicates that the onset of DC conduction is established by even reasonably short-ranged excursions of the cations",[58] and suppose that the barrier heights are small for large cation concentrations.

Following the consensus that DC conductivity and dispersion are part of one and the same process of ion hops, see reviews,[6,7] mean-square displacement of the mobile ions, $< r^2(t) >$, has been derived using a direct relation based on linear response theory[60,61] that involves a sine

transform of the derivative of the real-part of the experimental frequency-dependent conductivity spectra.[62-63] If the Haven ratio is assumed to be unity, since this is a hard to determine quantity, what this relation yields is $< R^2(t) >$, the mean-square displacement of the center of charge of the mobile ions. One thus constructs a plot of $log\langle R^2(t)\rangle$ versus $log(t)$, and can read off the value of $\langle R^2(t_p)\rangle$, where $t_p = 1/2\pi\nu_0$, corresponding to where ν_O marks the onset of conductivity-dispersion. The square root of this quantity is the characteristic length which marks crossover from sub-diffusive to diffusive motion of ions. A more general formula for determining $\langle R^2(t_p)\rangle^{1/2}$ using a simple power-law fitting of the conductivity spectra at low-frequencies has been subsequently outlined in Ref. 6.

Another length scale which is relevant is the spatial extent of localized diffusion, and is calculated as $\langle r_{loc}^2(\infty)\rangle^{1/2}$ from scaling of the real part of the permittivity spectra[7,45,46] using the MIGRATION concept; or in a model independent way from an analysis of the permittivity spectra[36,38,62,63] as $\langle R_{loc}^2(\infty)\rangle^{1/2}$. This length scale gives information on the nature of the localized excursions that the ion makes, and hence is closely related to local structure. It is *also* a material-specific temperature-independent property.

In contrast to the early findings of Sidebottom et al in 1997,[58] length scales in the other works were found to be several Angstroms in magnitude.[36,38,62,63] However, in MGFE systems studied by Zielniok et al,[16] as well as a re-analysis of their data by modelling the permittivity spectra Banhatti et al,[17] the values for spatial extent of localized hopping for sodium ion in borosphosphates similar in magnitude to what Sidebottom et al obtained.[58]

Appendix B   <u>The MIGRATION concept - details</u>

<u>*Leitmotif*</u>: The MIGRATION concept[7,45] uses a simple but realistic physical picture to describe the relaxation processes that ensue as a function of time in structurally disordered materials after following an elementary displacement of a central mobile ion from its site at $t = 0$ to a neighboring site. At $t = 0$ the ion was at its potential minimum, which is a superposition of single-particle potentials giving a cage minimum for the central ion under consideration.

Following a jump at $t = 0$, a mismatch is created between the new position of the ion and the momentary arrangement of its mobile neighbors. Thus, in materials with structural disorder, the jump relaxation at times $t > 0$ can be thus visualized along single- and many-particle routes: the ion moves backward along the single-particle route, while along the many-particle route its neighbors are
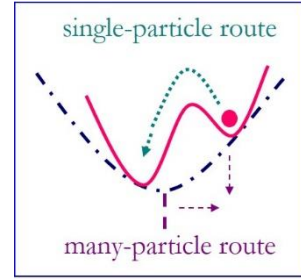

Figure A1: Schematic representation of the physical picture behind the MIGRATION concept.

rearranging. The schematic Fig. A1 shows the leitmotif of the model. Over time, this results in correlated forward-backward motion of the central ion.

<u>*Formulation of the Model*</u>: The functions $W(t)$ and $g(t)$ were introduced in the main text, and correspond to the functions that describe relaxations along the single- and many-particle routes respectively. At $t = 0, W(0) = g(0) = 1$; however, at long times the mismatch function has to decay, but a fraction of hops are successful: $W(\infty) \neq 0$, $g(\infty) = 0$. To precisely describe the decay of the mismatch function, a third function involving the number of mobile ions that respond to the dipole-field, $N(t)$, is needed, as it is time-dependent. However, $N(\infty) \neq 0$, since at no time

the nearest neighbours to the "central" ion can be shielded from the shrinking dipole field. The two rate equations and the third equation of the model are given by:

$$-\frac{\dot{W}}{W} = -B\dot{g}; \quad -\frac{\dot{g}}{g} = \Gamma_0 W(t) N(t); \quad N(t) - N(\infty) = [Bg(t)]^{K-1} \qquad \text{(A2-1)}$$

The proportionality constant of decay along the single-particle and many-particle routes is given by the relation. $B = -\ln(W(\infty))$. The parameter, Γ_0, is defined as the rate of elementary hops. The parameter K describes the nature of response to the hop of the "central" ion. For example, if the response of the neighborhood is collective, as in a melt or a liquid electrolytes, then, K is closer to 1 and $N(t)$ is time-independent and equal to $N(\infty)$. However, for $K > 1$, the decay of $N(t)$ is proportional or faster than $g(t)$, and is exactly equal to $g(t)$ for $K = 2$.

It is advantageous to switch to a scaled notation as it yields a master curve, and this is correlated to scaling features displayed by the experimental spectra. Thus, $W_s(t_s) := W(t_s)/W(\infty)$, $t_s :=$ $t \cdot \omega_O$ & $\omega_s = \omega/\omega_O$. Here, ω_O is defined by $\omega_O = \Gamma_0 \cdot W(\infty) = \Gamma_0 \cdot \exp(-B)$, and is defined as the "rate of successful hops". A numerical solution to the set of equations denoted as Eq. (A2-1) is obtained on solving the equation:

$$-\frac{dW_s(t_s)}{dt_s} = W_s^2(t_s) \cdot \ln(W_s(t_s)) \cdot \{(\ln(W_s(t_s)))^{K-1} + N(\infty)\} \qquad \text{(A2-2)}$$

Connection to Conductivity Spectra: Linear response theory provides a link between frequency-dependent conductivities and correlation functions describing the ion dynamics.[60,61] The frequency-dependent conductivity is proportional to the Fourier transform of the time-dependent auto-correlation function of the current density, $< \iota(0) \cdot \iota(t) >$. This autocorrelation function may be written as:

$$< \iota(0) \cdot \iota(t) >= V^{-2} \sum_{i,j}^{1..N} q_i q_j \cdot < v_i(0) \cdot v_j(t) >. \qquad \text{(A2-3)}$$

Here, V is the volume of the sample, N is the total number of ions in the sample, q and v denote charge and velocities and summation is over both i & j. Eq. (A2-3) is considerably simplified, if all mobile ions are of the same kind with charge q, and if we ignore the cross-correlation terms so that a Fourier transform of it yields the complex conductivity spectra corresponding to the hopping contribution, $\hat{\sigma}_{hop}(\omega)$:

$$\hat{\sigma}_{hop}(\omega) = \frac{Nq^2}{3Vk_BT} \int_{0^-}^{\infty} < \mathbf{v}(0) \cdot \mathbf{v}(t) >_{hop} \exp(-i\omega t) \tag{A2-4}$$

Returning to the current density autocorrelation function, it can be shown that it has a sharp positive peak at very short times where relaxations do not yet play a role, and is negative at later times and decays to zero at long times. It has been shown in detail in Ref. 64 that the time-derivative of our model function, $\dot{W}(t)$, when suitably normalised, is equivalent to the time-derivative of the response function which is proportional to the current density autocorrelation function in linear response theory. This implies that when cross terms are ignored in Eq. (A2-3), $W(t)$ becomes the normalized integral of the velocity auto-correlation function and thus, at the same time, the normalized time derivative of the mean square displacement of the mobile ions. Using the definition of $W(t)$ as a normalised integral of velocity autocorrelation function, Eq. (A2-4) can be combined with the solution of (A2-2), to yield scaled model conductivity- and permittivity-spectrum using the Fourier transform Eqs. (1) & (2) of main text.

Estimation of the Spatial Extent of Localized Diffusion: Using the definition that $W(t)$ is the normalized time derivative of the mean square displacement of the mobile ions, we write[17,45-46]

$$\langle r^2(t) \rangle_S = \int_0^{t_S} [W_S(t'_S)] \cdot dt'_S = \omega_O \frac{\langle r^2(t) \rangle}{6D}. \tag{A2-5}$$

Here D is the self-diffusion coefficient. At long times the mean-square displacement of the ions becomes diffusive, giving $\langle r^2(\infty) \rangle_S = t_S$. Eq. (A2-5) can be used to define the spatial extent of localized motion of ions as:

$$\langle r_{loc}^2(t) \rangle_S = \int_0^{t_S}(W_s(t'_s) - 1) \, dt'_s = \omega_O \frac{\langle r^2(t) \rangle - 6Dt}{6D} \tag{A2-6}$$

Relating Eq.(A2-6) to Eq. (3), and using analogy to Eq. (A2-5), it can be shown that[17]

$$\langle r_{loc}^2(\infty) \rangle = 6D \frac{\varepsilon_S(0)}{\omega_O} \tag{A2-7}$$

Equation (A2-7) can be further written as a temperature-independent and a material property using Nernst-Einstein relation as:

$$\langle r_{loc}^2(\infty) \rangle = \frac{6k_B \sigma_{DC} T}{N_v q^2} \cdot \frac{\varepsilon_S(0)}{\omega_O} \tag{A2-8}$$

This is also given as Eq. 4 in main text.

Parameters of the model: To construct a model conductivity spectrum, we need to specify two parameters, B and K while solving Eq. (A2-2). The parameter K describes the shape of the conductivity spectra at the onset of conductivity dispersion. The parameter B is a measure of the height of conductivity dispersion. From model, we know that $W(\infty) = \exp(-B)$. On Fourier transformation, we find that $W(\infty) = \sigma_{DC}/\sigma_{HF}$, where σ_{HF} is the conductivity plateau that can be measured at very short times (high frequencies) of all elementary hops, if not swamped by vibrational components.[7] For modelling the experimental conductivity spectra obtained from impedance spectroscopy B can be arbitrarily chosen since the frequency range is much below where σ_{HF} can be observed. Further, such an arbitrary choice of B is justified by the fact that the value of B does not influence the shape of the spectrum – see right panel of Fig. A2.

The third parameter, $N(\infty)$ is crucial for modelling the scaled permittivity spectrum, as the value of $W_S(t_S) - 1$ as given in Eqs. (1) & (2) of main text is small around the onset of conductivity dispersion. If at all, it can affect the value below the onset region, but this effect is marginal. While in
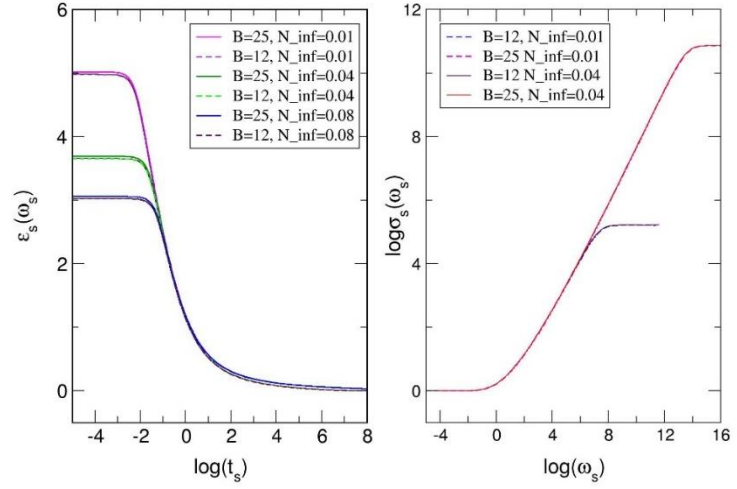

Figure A2: The effect of variation of the values of parameters B and $N(\infty)$ for a given value of K on the model permittivity (left) and conductivity spectra (right). See text for details.

Eq. (1), the sine term is also small at this regime, in Eq. (2), the cosine term is equal to 1, so that a suitable value of $N(\infty)$ in Eq. (A2-2) is needed to determine the height of the scaled permittivity plateaux. There is no direct relation from the model between the value of $N(\infty)$ and $\varepsilon_S(0)$, except the observed reverse correlation that $\varepsilon_S(0)$ increases as $N(\infty)$ decreases. Moreover, the value of B affects this height but very marginally, and this variation is well within the error bars when used in determining the plateau of experimental permittivity spectra. All these above described features of the model parameters are illustrated in the left panel of Fig. A2, where conductivity and permittivity model spectra have been constructed for $K = 2$, using for B, the values 12 and 25; similarly, different values of $N(\infty)$ has been used.

.

ASSOCIATED CONTENT

Supporting Information.

Filename SI-MGF-systemsA+B-Sklepic-etal.docx (5 figures and three tables)

S1 Details of results on System A: $40Li_2O-(60-x)P_2O_5-xGeO_2$ glasses with x = 0 to 25 mol%

S1.1 Thermal behaviour

S1.2 Electrical Properties

S2 Additional details of NMR results from 1D/2D $^{31}P/^{11}B$ NMR for System B: $40Li_2O-10B_2O_3-(50-x)P_2O_5-xGeO_2$, x = 0 to 25 mol%

S3 Information on number density, model parameters describing the conductivity and permittivity spectra and relevant length scales of ion dynamics in systems A and B

AUTHOR INFORMATION

Corresponding Author

Dr. Radha D. Banhatti

*rbanhatt@irb.hr

Author Contributions

The manuscript was written through contributions of all authors. All authors have given approval to the final version of the manuscript. All authors contributed equally to various parts of the manuscript.

ACKNOWLEDGMENT

REFERENCES

1. Funke, K. Solid State Ionics: from Michael Faraday to Green Energy – the European Dimension. *Sci. Technol. Adv. Mater.* **2016**, *14:4*, 043502

2. Cao, C.; Li, Z. B.; Wang, X. L.; Zhao, X. B.; Han, W. Q. Recent Advances in Inorganic Solid Electrolytes for Lithium Batteries. *Front. Energy Res.* **2014**, *2*, 25(1-10.)

3. Duclot, M.; Souquet. J. L. Glassy Materials for Lithium Batteries: Electrochemical Properties and Devices Performances. *J. Power Sources* **2001**, *97*, 610-615.

4. Lindic, M. H.; Pecquenard, B.; Vinatier, P.; Levasseur, A.; Martinez, H.; Gonbeau, D.; Petit, P. E.; Ouvrard, G. Electrochemical Mechanisms During Lithium Insertion into $TiO_{0.6}S_{2.8}$ Thin Film Positive Electrode in Lithium Microbatteries. *Journal of The Electrochemical Society* **2005**, *152.1*, A141-A146.

5. Dudney, N. J. *Glass and Ceramic Electrolytes for Lithium and Lithium-Ion Batteries in Lithium Batteries: Science and Technology*; G. Abbas Nazri and G. Pistoia (Eds.), Springer, New York, USA, 2003.

6. Dyre, J. C.; Maass, P.; Roling, B.; Sidebottom, D. L. Fundamental Questions Relating to Ion Conduction in Disordered Solids. *Rep. Prog. Phys.* **2009**, *72.4*, 046501

7. Funke, K.; Banhatti, R. D.; Laughman, D.M.; Badr, L.G.; Mutke, M.; Santic, A.; Wrobel, W.; Fellberg, E. M.; Biermann, C. First and Second Universalities: Expeditions Towards and Beyond. *Z. Phys. Chem.* **2010**, *224.10-12*, 1891-1950.

8. Ingram, M. D. Ionic Conductivity in Glass. *Phys. Chem. Glasses* **1987**, *28*, 215-234.

9. Ingram, M. D. Ionic Conductivity and Glass Structure. *Philos. Mag.* **1989**, *60(6)*, 729-740.

10. Bunde. A.; Ingram, M. D.; Maass, P. The Dynamic Structure Model for Ion Transport in Glasses. *J. Non-Cryst. Solids* **1994**, *172*, 1222-1236.

11. Magistris, A.; Chiodelli, G.; Villa, M. Lithium Borophosphate Vitreous Electrolytes. *J. Power Sources* **1985**, *14(1)*, 87-91.

12. Deshpande, V. K.; Pradel, A.; Ribes, M. The Mixed Glass Former Effect in the $Li_2S:SiS_2:GeS_2$ System. *Mater. Res. Bull.* **1988**, *23.3*, 379-384.

13. Salodkar, R. V.; Deshpande, V. K.; Singh K. Enhancement of the Ionic Conductivity of Lithium Borophosphate Glass: a Mixed Glass Former Approach. *J. Power Sources* **1989**, *25.4*, 257-263.

14. Chowdari, B. V. R.; Rong. Z. The Influence of Bi_2O_3 on $yLi_2O \cdot (1-y)\{xBi_2O_3(1-x)B_2O_3\}$ Glass System. *Solid State Ionics* **1998**, *86*, 527-533.

15. Zielniok, D.; Cramer, C.; Eckert, H.; Structure/Property Correlations in Ion-Conducting Mixed-Network Former Glasses: Solid-State NMR Studies of the System Na_2O-B_2O_3-P_2O_5. *Chem. Mater*. **2007**, *19*, 3162-3170.

16. Zielniok, D.; Eckert H.; Cramer. C. Direct Correlation between Nonrandom Ion Hopping and Network Structure in Ion-Conducting Borophosphate Glasses. *Phys. Rev. Lett.* **2008**, *100.3*, 035901(1-4.)

17. Banhatti, R. D.; Cramer, C.; Zielniok, D.; Robertson, A. H.; Ingram, M. D. Insights into Ion-Network Interactions and Ion Transport in Glass. *Z. Phys. Chem.* **2009**, *223.10-11*, 1201-1215.

18. Raskar, D.; Rinke, M. T.; Eckert, H. The Mixed-Network Former Effect in Phosphate Glasses: NMR and XPS Studies of the Connectivity Distribution in the Glass System $(NaPO_3)_{1-x}$ $(B_2O_3)_x$. *J. Phys. Chem. C* **2008**, *112*, 12350-12539.

19. Rinke, M. T.; Eckert, H. The Mixed Network Former Effect in Glasses: Solid State NMR and XPS Structural Studies of the Glass System $(Na_2O)_x(BPO_4)_{1-x}$. *Phys. Chem. Chem. Phys*. **2011**, *13*, 6552-6565.

20. Raguenet, B.; Tricot, G.; Silly, G.; Ribes, M.; Pradel, A. Revisiting the 'Mixed Glass Former Effect' in Ultra-Fast Quenched Borophosphate Glasses by Advanced 1D/2D Solid State NMR. *J. Mat. Chem*. **2011**, *21*, 17693-17704.

21. Christensen, R.; Byer, J.; Olsen, G.; Martin, S. W. The Glass Transition Temperature of Mixed Glass Former $0.35Na_2O + 0.65[xB_2O_3 + (1-x)P_2O_5]$ glasses. *J. Non-Cryst. Solids* **2012**, *358*, 826-831.

22. Christensen, R.; Olsen, G.; Martin, S. W. Structural Studies of Mixed Glass Former $0.35Na_2O + 0.65[xB_2O_3 + (1–x)P_2O_5]$ Glasses by Raman and ^{11}B and ^{31}P Magic Angle Spinning Nuclear Magnetic Resonance Spectroscopies. *J. Phys. Chem. B* **2013**, *117*, 2169-2179.

23. Tho, T. D.; Prasada Rao, R.; Adams, S. Structure Property Correlation in Lithium Borophosphate Glasses. *Eur. Phys. J.* **2012**, *35*, 8(1-11.)

24. Karlsson, M.; Schuch, M.; Christensen, R.; Maass, P.; Martin, S. W.; Imberti, S.; Matic, A.; Structural Origin of the Mixed Glass Former Effect in Sodium Borophosphate Glasses Investigated with Neutron Diffraction and Reverse Monte Carlo Modeling. *J. Phys. Chem. C* **2015**, *119*, 27275-27284.

25. Larink, D.; Eckert, H.; Reichert, M.; Martin, S. W. Mixed Network Former Effect in Ion-Conducting Alkali Borophosphate Glasses: Structure/Property Correlations in the System $[M_2O]_{1/3}[(B_2O_3)_x(P_2O_5)_{1–x}]_{2/3}$ (M= Li, K, Cs). *J. Phys. Chem. B* **2012**, *116*, 26162-26176.

26. Storek, M.; Bohmer, R.; Martin, S. W.; Larink, D.; Eckert, H. NMR and Conductivity Studies of the Mixed Glass Former Effect in Lithium Borophosphate Glasses. *J. Chem. Phys.* **2012***, 137*, 124507(1-12.)

27. Tho, T. D.; Prasada Rao, R.; Adams, S. Glass Formation, Structure and Ion Transport in $0.45Li_2O–(0.55–x)P_2O_5–xB_2O_3$ Glasses." *Phys. Chem. Glasses: Eur. J. Glass Sci. Technol., Part B* **2011**, *52*, 91-100.

28. Christensen, R.; Olsen, G.; Martin, S.W. Ionic Conductivity of Mixed Glass Former $0.35Na_2O + 0.65[xB_2O_3 + (1–x)P_2O_5]$ Glasses. *J. Phys. Chem. B* **2013**, *117*, 16577-16586.

29. Tricot, G.; Raguenet, B.; Silly, G.; Ribes, M.; Pradel, A.; Eckert, H. P-O-B^3 Linkages in Borophosphate Glasses Evidenced by High Field 11B/31P Correlation NMR. *Chem. Comm.* **2015**, *51*, 9284-9286.

30. Osaka, A.; Jianrong, Q.; Miura, Y.; Yao, T. EXAFS of Germanium in Glasses of the GeO_2 – TeO_2 System. *J. Non-Cryst. Solids* **1995**, *191*, 339-345.

31. Kumar, S.; Murugavel, S.; Rao, K. J. Absence of Germanate Anomaly in Ternary Lithium Germanophosphate Glasses: Modification Behaviour of Mixed Glass System of Strong and Fragile Formers. *J. Phys. Chem. B* **2001**, *105*, 5862-5873.

32. Kumar, S.; Rao, K. J. Lithium Ion Transport in Germanophosphate Glasses. *Solid State Ionics* **2004**, *170*, 191-199.

33. Zwanziger, J. W.; Shaw, J. L.; Werner-Zwanziger, U.; Aitken, B.G. A Neutron Scattering and Nuclear Magnetic Resonance Study of the GeO_2–P_2O_5 Glasses. *J. Phys. Chem. B* **2006**, *110*, 20123-20128.

34. Hoppe, U.; Wyckoff, N. P.; Brow, R. K.; von Zimmermann, M.; Hannon, A.C. Structure of Na_2O–GeO_2–P_2O_5 Glasses by X-ray and Neutron Diffraction. *J. of Non-Cryst. Solids* **2014**, *390*, 59–69.

35. Behrends, F.; Eckert. H. Mixed Network Former Effects in Oxide Glasses: Spectroscopic Studies in the System $(M_2O)_{1/3}[(Ge_2O_4)_x(P_2O_5)_{1-x}]_{2/3}$. *J. of Phys. Chem. C* **2014**, *118*, 10271-10283.

36. Kabi, S.; Ghosh, A. Silver Ion Dynamics In Mixed Network Former Glasses: Evidence of Correlation with Characteristic Lengths and Network Structure. *EPL* **2012**, *100.2*, 26007(1-5.)

37. Shaw, A.; Ghosh, A. Correlation of Microscopic Length Scales of Ion Dynamics with Network Structure in Lithium-Iodide-Doped Lithium Metaphosphate Glasses. *EPL* **2013**, *100*, 66003(1-6.)

38. Shaw, A.; Ghosh, A. Correlation of Ion Dynamics with Characteristic Length Scales and Network Structural Units in Bismuth Borate Glasses. *J. Chem. Phys.* **2013**, *139.11*, 114503(1-8.)

39. Wang, Q.; Hu, B.; Lafon, O.; Trebosc, J.; Deng, F.; Amoureux, J. P. Double-Quantum Homonuclear NMR Correlation Spectroscopy of Quadrupolar Nuclei Subjected to Magic-Angle Spinning and High Magnetic Field. *J. Magn. Reson.* **2009**, *200.2*, 251-260.

40. Tricot, G.; Trebosc, J.; Pourpoint, F.; Gauvin, R.; Delevoye, L. The D-HMQC MAS-NMR Technique: An Efficient Tool for the Editing of Through-Space Correlation Spectra Between Quadrupolar and Spin-1/2 (31P, 29Si, 1H, 13C) Nuclei. *Annual Report on NMR spectroscopy*, **2014**, *81*, 145-184.

41. Eckert, H. Network Former Mixing (NFM) Effects in Ion-Conducting Glasses-Structure/Property Correlations Studied by Modern Solid-State NMR Techniques. *Diffus. Found.* **2015**, *6*, 144-193.

42. Murthy, M. K.; Kirby, E. M. Infra-Red Spectra of Alkali-Germanate Glasses. *Phys. Chem. Glasses* **1964**, *5*, 144-146.

43. Price, D. L.; Ellison, A. J. G.; Saboungi, M. L.; Hu, R. Z.; Egami, T.; Howells, W. S. Short-, Intermediate-, and Extended-Range Order in Rubidium Germanate Glasses. *Phys. Rev. B* **1997**, *55*, 11249-11255.

44. Moguš-Milanković, A.; Sklepić, K.; Mošner, P.; Koudelka, L.; Kalenda, P. Lithium-Ion Mobility in Quaternary Boro-Germano–Phosphate Glasses. *J. Phys. Chem. B* **2016**, *120.16*, 3978-3987.

45. Funke, K.; Banhatti, R. D. Modelling Frequency-Dependent Conductivities and Permittivities in the Framework of the MIGRATION Concept. *Solid State Ionics* **2004**, *169.1*, 1-8.

46. Banhatti, R. D.; Funke, K. Dielectric Function and Localized Diffusion in Ion Conducting Glasses. *Solid State Ionics* **2004**, *175.1*, 661-663.

47. Funke, K. Jump Relaxation in Solid Electrolytes. *Prog. Solid State Chem.* **1993**, *22*, 111-195.

48. Funke, K.; Banhatti, R. D.; Brückner, S.; Cramer, C.; Krieger, C.; Mandanici, A.; Martiny, C.; Ross, I. Ionic Motion in Materials with Disordered Structures: Conductivity Spectra and the Concept of Mismatch and Relaxation. *Phys. Chem. Chem. Phys.* **2002**, *4*, 3155-3167.

49. Summerfeld, S. Universal Low-Frequency Behaviour in the ac Hopping Conductivity of Disordered Systems. *Phil. Mag. B* **1985**, *52*, 9-22.

50. Sidebottom, D. L. Universal Approach for Scaling the ac Conductivity in Ionic Glasses. *Phys. Rev. Lett.* **1999**, *82*, 3653-3656.

51. Mošner, P.; Vorokhta, M.; Koudelka, L.; Montagne, L.; Revel, B.; Sklepić, K.; Moguš-Milanković, A. Effect of Germanium Oxide on the Structure and Properties of Lithium Borophosphate Glasses. *J. Non-Cryst. Solids* **2013**, *375*, 1-6.

52. Henderson, G.S. The Germanate Anomaly − What Do We Know? *J. Non-Cryst. Solids* **2007**, *353*, 1695-1704.

53. Evastropiev, K. S.; Ivanov O. A. *Advances in Glass Technology, Part 2*; Eds.: F.R. Matson, G.E. Rindone; Plenum: New York, 1963.

54. Nelson, B. N.; Exarhos, G. J. Vibrational Spectroscopy of Cation-Site Interactions in Phosphate Glasses. *J. Chem. Phys.* **1979**, *71*, 2739-2747.

55. Takahashi, K.; Mochida, N.; Matsui, H.; Gohshi, Y. Properties and Structure of Glasses in the Systems Silicon Oxide-Phosphate (SiO_2-$PO_{5/2}$) and Germanate Oxide-Phosphate (GeO_2- $PO_{5/2}$). *J. Ceramic. Soc. Jpn.* **1976**, *84*, 482-488.

56. Hannon, A. C.; Di Martino, D.; Santos, L. F. Almeida, R. M. Ge-O Cordination in Cesium Germanate Glasses. *J. Phys. Chem. B* **2007**, *111*, 3342-3354.

57. Hannon, A. C.; Di Martino, D.; Santos, L. F. Almeida, R. M. A Model for the Ge-O Coordination in Germanate Glasses. *J. Non-Cryst. Solids* **2007**, *353*, 1688-1694.

58. Sidebottom, D.L.; Green, P.F.; Brow, B.K.; Structural Correlations in the ac Conductivity of Ion-Containing Glasses. *J. Non-Cryst. Solids* **1997**, *222*, 354-360.

59. Murugavel, S.; Roling, B. Ionic Transport in Glassy Networks with High Electronic Polarizabilities: Conductivity Spectroscopic Results Indicating a Vacancy-Type Transport Mechanism. *J. of Phys. Chem. B* **2004**, *108*, 2564-2567.

60. Kubo, R. The Fluctuation-Dissipation Theorem. *Rep. on Prog. In Phys.* **1966**, *29(1)*, 255-284.

61. Kubo, R. Statistical-Mechanical Theory of Irreversible Processes. I. General Theory and Simple Applications to Magnetic and Conduction Problems. *J. Phys. Soc. Jpn.* **1957**, *12*, 570-586.

62. Roling, B.; Martiny, C.; Funke, K. Information on the Absolute Length Scales of Ion Transport Processes in Glasses from Electrical Conductivity and Tracer Diffusion Data. *J. Non-Cryst. Solids* **1999**, *249*, 201-209.

63. Roling, B.; Martiny, C.; Brueckner, S.; Ion Transport in Glass: Influence of Glassy Structure on Spatial Extent of Non-Random Ion Hopping. *Phys. Rev. B* **2001**, *63*, 214203(1-9.)

64. Funke, K.; Banhatti, R.D. Translational and Localised Ionic Motion in Materials with Disordered Structures. *Solid State Sci.* **2008**, *10*, 790-803.

TOC graphic